Autogenous self-healing of low embodied energy cementitious materials: Effect of multi-component binder and crack geometry

Magdalena Rajczakowska [a,*], Ilda Tole [a], Hans Hedlund [a,b], Karin Habermehl-Cwirzen [a], Andrzej Cwirzen [a]

[a] Building Materials, Department of Civil, Environmental, and Natural Resources Engineering, Luleå University of Technology, 971 87 Luleå, Sweden
[b] Skanska Sverige AB, 40518 Göteborg, Sweden

ARTICLE INFO

ABSTRACT

Concrete's ability to auto-repair the cracks reduces the need for maintenance and repair. Autogenous self-healing is an intrinsic property of concrete highly dependent on the binder composition. The urgent necessity to decrease CO_2 emissions of concrete by replacing cement with "greener" materials provides challenges and opportunities for self-healing cementitious materials. This research aims to verify the self-healing behavior of environmentally friendly multi-component binders. An experimental study is conducted to test the effect of binder composition-related parameters (e.g., phase composition, porosity) and crack geometry on the self-healing efficiency of the "green" mortars. Cementitious materials with 50 wt.%cement replacement with limestone powder blended with fly ash, blast furnace slag, and silica fume are investigated. Sorptivity change, compressive strength regains, and crack closure after self-healing are used to quantify the self-healing efficiency. Quantitative analysis and correlations between chemical composition/microstructural features, geometrical crack characteristics, and self-healing measures are investigated. The results indicate that "green" binder composition affects the self-healing mechanism leading to different levels of performance recovery. Some SCMs-limestone binder formulations enable a better self-healing efficiency than pure OPC or OPC/limestone cementitious materials, presumably due to a synergistic effect between the limestone and the mineral additions. Correlation analysis indicated that geometrical complexity characterized by fractal dimension and tortuosity of the crack does not affect the external crack closure, whereas the fractal dimension and maximum crack width are correlated with the internal crack healing.

1. Introduction

Buildings contribute to approximately 40% of total energy consumption [1]. Recent studies show that embodied energy (EE), included in manufacturing materials and life cycle processes, can reach even 46% of total energy consumption [2]. An essential part of EE is the recurrent embodied energy (REE) used for life cycle maintenance and repair processes which are equal to or even higher than initial embodied energy (IEE) connected to manufacturing and construction processes. Therefore, it is critical to reduce the buildings' REE by developing materials with long service life.

Cementitious materials are brittle and prone to cracking, which causes structural problems and shortens the service life of structures. Therefore, maintenance and repairs necessary throughout the lifetime of a concrete structure contribute to an increased REE. The latest research

led to the development of "smart" functional cementitious materials with extended service life, achieved by, e.g., self-healing properties. Concrete has an in-built ability to self-repair cracks up to 150 µm [3], the efficiency of which can be improved with, e.g., the addition of certain types of fibers or specific exposure conditions [4]. Preliminary life cycle assessment (LCA) of self-healing concrete shows that a self-healing concrete structure would require repairs only after 60–94 years compared to 7 years for an ordinary concrete slab. As a result, the environmental impact of the material would be reduced by 56%–75% [5].

Approximately 8 billion cubic meters of concrete are produced yearly, corresponding to 1 m^3 per person [6]. In 2015, ordinary Portland cement (OPC) production reached 4,6 billion tonnes, 34 times more than in the 1950s [7]. The production process of OPC involves calcination and grinding that generate approximately 842 kg of CO_2 per tonne of

clinker. All these combined make concrete responsible for 6–10% of the total anthropogenic greenhouse gas emissions [8]. One tonne of carbon dioxide today, in terms of emission targets, is different from 50 years from now due to target emission changes. "Time Value of Carbon" makes the construction industry transformation even more pressing [9]. The necessity to decrease concrete CO_2 emissions demands replacing cement binders with "greener" materials, e.g., limestone, industrial by-products, i.e., fly ash, and blast furnace slag. At the same time, mix composition changes affect concrete's autogenous self-healing performance [10].

Limestone is a locally available low-cost material that gives beneficial characteristics to cementitious composites, e.g., carbonate-AFm phases are more stable than the sulfate AFm phases preventing the decomposition of ettringite to monosulphate [11]. Limestone accelerates the reaction of cement by providing a surface for the nucleation of hydration products [12]. The amount that can react is limited by the transport of ions, Al and Ca, which can be decreased by, e.g., a dense hydrated binder matrix. On the other hand, too much limestone can reduce the later strength by the "dilution effect" [13]. The so-called Limestone Calcined Clay Cement (LC3) binders with calcined clay and limestone have attracted lots of attention recently due to their excellent performance and reduced environmental impact [14]. Ternary and quaternary systems are investigated with other SCMs, e.g., fly ah and slag, to optimize the mix performance while reducing CO_2 emissions [15]. These multi-component binders exhibit changes concerning the pore network and phase assemblage compared to binary mixes, which affects their macroscopic properties, including the self-healing behavior.

Mineral admixtures generally promote the self-healing process [16]. For instance, binary cementitious materials with partial cement replacement with 10 wt% silica fume, 30 wt% pulverized fuel ash and 50 wt% ground granulated blast-furnace slag demonstrate enhanced self-healing behavior at 28 days after water exposure. Different governing mechanisms are suggested depending on the SCM type [17], e.g., ongoing hydration or calcite precipitation. On the other hand, negative results, compared with pure OPC, are observed for fly ash and blast-furnace slag binary composites when cracked at an early age [18]. An increase in the SCMs content is unfavorable, possibly due to the lower amount of Portlandite consumed by the pozzolanic reaction with SCMs [18].

Several studies concern the self-healing performance of binary cementitious materials (e.g., [19–21]); however, there is scarce data on the performance of the multi-component binder systems despite their significant economic and environmental benefits. For example, ternary binders with slag and metakaolin exposed to water exhibit more efficient self-healing for narrow early-age cracks [22]. On the other hand, composites with slag and limestone/siliceous filler show improved self-healing at an older age after 28 days of curing [23].

The self-healing process is dependent not only on the binder composition but also on the geometry of the crack-to-be-healed. The healing efficiency is often described in relation to the width of the crack opening (e.g., [24]). Nevertheless, this is a simplification since the crack usually has a complex shape. The crack geometry is proven to influence the transport properties of cementitious materials, e.g., chloride penetration [25]. The crack complexity can be represented by more sophisticated microstructural properties, e.g., tortuosity [26] or fractal dimension [27]. However, despite the potential significance of these features, there is a lack of studies that combine the effect of the binder composition and crack complexity on the autogenous self-healing process.

The objective of this research is to verify the self-healing behavior of environmentally friendly multi-component binders. Fifteen mortars are investigated with a binder composed of OPC mixed with limestone, fly ash, slag, and silica fume, in different proportions. The effect of microstructure, chemical composition, and crack geometry on the self-healing efficiency is studied. Sorptivity change, compressive strength regains, and crack closure after self-healing is used to describe the self-healing efficiency of the materials (Fig. 1).

2. Materials and methods

2.1. Materials selection

The sources of popular SCMs, i.e., fly ash (FA) and slag (S), commonly used as a cement replacement to decrease the CO_2 emissions of concrete, are limited [28]. In contrast, limestone (LM) is plentifully available, with low embodied energy and half of the CO_2 emissions released compared to OPC [29–31]; therefore, blended cementitious binders based on LM and SCMs could be a reasonable choice for environmentally friendly cementitious materials. However, there is scarce data on the self-healing of LM-based multi-component binders. Therefore, in this study, several "extreme" mix compositions were selected to
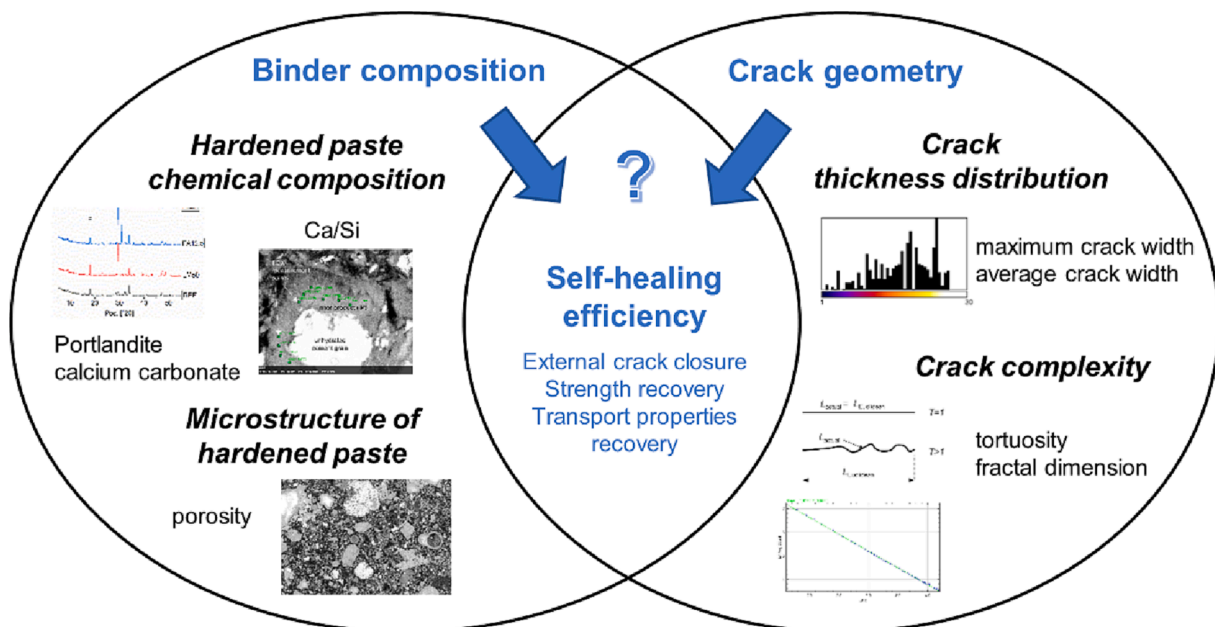

Fig. 1. Overview of the experimental setup.

explore their potential concerning autogenous self-healing at an early age. In addition to a reduced carbon footprint, specific characteristics of LM-SCM binder systems could have a substantial effect on the self-healing properties:

- At an early age, adding limestone increases the hydration reaction rate resulting in more $Ca(OH)_2$,[32] presumably an essential supply of the calcium ions due to leaching when the material is exposed to water, which could also favor the self-healing process. Furthermore, the formation of new calcite during the calcium leaching process was observed for the specimens with $CaCO_3$ addition [33]. This phenomenon could potentially promote a self-healing mechanism by calcite precipitation.
- Amounts of LM up to 15 wt% of cement are used as a filler to improve concrete properties; however, above 15 wt% results in higher open porosity and permeability [34], partially due to the dilution effect [35]. Permeable binder matrix and interconnectivity of the pore network are factors potentially facilitating the transport of ions into the crack during the self-healing process [10]. On the other hand, combining LM with SCMs could lead to an increased pozzolanic reaction, resulting in a dense binder matrix with low porosity, hindering the transfer of ions into the crack.
- Hydration of cementitious binders with high amounts of limestone and SCMs leads to distinct phase assemblage and microstructural features, especially at an early age, with pros and cons regarding autogenous self-healing. For instance, although a higher amount of $Ca(OH)_2$ enables the pozzolanic reaction of SCMs, it could result in a low concentration of Ca^{2+} ions inside the crack due to portlandite depletion. In contrast, a smaller amount of $Ca(OH)_2$ may impose a higher diffusion rate of calcium from the hydrated binder into the crack caused by a low calcium-pore solution and resulting high concentration gradient when exposed to water.

2.2. Materials

Mortar and paste were prepared using ordinary Portland cement (OPC) CEM I 42.5 N produced by Cementa (Skövde, Sweden). Cement was replaced by a mixture of limestone (LM), fly ash (FA), blast furnace slag (S), and silica fume (SF). Australian low-calcium (Class F) FA and German slag (S) provided by Thomas Cement from Bremen, Germany, were used. Oxide compositions of all the materials are listed in Table 1. Elkem Microsilica (Oslo, Norway) Grade 920D (SF) and limestone powder Nordkalk Limus 40 from Nordkalk AB were used. Grading curves of limestone and SCMs are shown in Fig. 2. The fine aggregate, i.e., river sand, provided by Baskarpsand AB (Habo, Sweden) with particles smaller than 1 mm was used.

Polypropylene (PP) fibers, with a diameter equal to around 0.025 mm and a length of approximately 5 mm, were used in the amount of 0.5 wt% of the binder. The main reason for the fiber application was to control the width of the crack opening during crack induction. A higher dosage of certain polymer fibers was previously observed to enhance the self-healing properties by acting as nucleation sites for the formed phases [36]. Nevertheless, in the case of this study, this effect was not the primary objective. Therefore, a relatively small amount of PP fibers

Table 1
Chemical composition of the OPC, SCMs, and limestone.

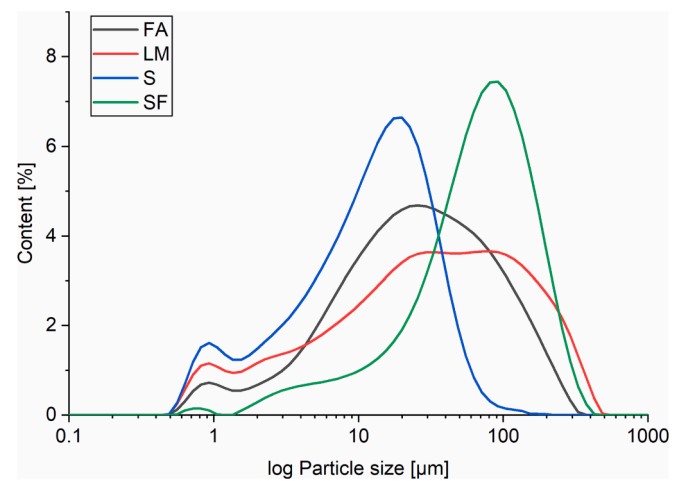| Oxide	OPC	FA	S	LM	SF
	Mean value (%)				
SiO_2	21.20	65.9	37.9	5.91	97.7
Al_2O_3	3.40	24.0	13.2	1.23	0.17
CaO	63.30	1.59	38.5	50.9	0.22
Fe_2O_3	4.10	2.87	0.37	1.49	0.19
K_2O	0.56	0.58	0.641	0.28	0.44
LOI	2.5	1.8	0.5	37.6	0.89

Fig. 2. Particle size distribution of SCMs and limestone.

was chosen since their lack of polarity made them neutral, considering the self-healing process [36].

Fifteen binder compositions were used to prepare the cementitious materials (Table 2). Mortars had a water-to-binder ratio of 0.4, and a sand-to-binder ratio of 1:1. The same binder composition and the water-to-binder ratio were kept for the paste samples. It should be noted that a non-standard mortar composition with a lower amount of fine aggregate could lead to an increased self-healing performance due to a higher amount of unhydrated binder exposed by a crack.

Mixing of the mortar specimens was done with a Hobart mixer. First, dry ingredients were mixed for 1 min, followed by mixing with water for 2 min. Finally, the PP fibers were added, and the material was mixed for 1 min. Afterward, the specimens were cast into standard 4 cm × 4 cm × 16 cm steel molds and vibrated on the vibrating table for 40 s. The beams were demolded after 24 h and cured in a water tank at approximately 20 °C for 7 days. In total, 135 specimens were prepared, nine per mix composition.

The paste was prepared using a vacuum mixer, type Bredent. The binder ingredients (Table 2) and water were mixed in the mixing beaker at 390 rpm for 2 min. The paste was placed in cylindrical polypropylene molds with a diameter of 33 mm. The container was sealed for 7 days to prevent moisture evaporation from the material.

Table 2
Binder proportions for mortar and paste samples.

#	Mix	OPC (g)	LM (g)	FA (g)	S (g)	SF (g)
Mix 1	REF	1000	0	0	0	0
Mix 2	LM50	500	500	0	0	0
Mix 3	LM43.75 FA6.25	500	437.5	62.5	0	0
Mix 4	LM37.5 FA12.5	500	375	125	0	0
Mix 5	LM25 FA25	500	250	250	0	0
Mix 6	LM43.75 S6.25	500	437.5	0	62.5	0
Mix 7	LM37.5 S12.5	500	375	0	125	0
Mix 8	LM25 S25	500	250	0	250	0
Mix 9	LM43.75 SF6.25	500	437.5	0	0	62.5
Mix 10	LM37.5 SF12.5	500	375	0	0	125
Mix 11	LM25 SF25	500	250	0	0	250
Mix 12	LM25 FA12.5 S12.5	500	250	125	125	0
Mix 13	LM25 FA12.5 SF12.5	500	250	125	0	125
Mix 14	LM25 S12.5 SF12.5	500	250	0	125	125
Mix 15	LM12.5 FA12.5 S12.5 SF12.5	500	125	125	125	125

2.3. Methods

2.3.1. Crack induction

Two types of tests were used to induce damage in the mortar specimens, i.e., the three-point bending test and the compression test. The following procedure was maintained for all the mixes.

Three beams were cracked at 7 days using a three-point bending test with a constant loading rate of 0.5 mm/min following a procedure similar to EN 1015-11:2019 [37]. A universal loading machine with displacement control, type Wykeham Farrance, with a 50 kN loading cell combined with the QuantumX MX440B universal measuring amplifier (HBM, Darmstadt, Germany) was used. A maximum crack opening of approximately 300 μm was controlled by a digital optical microscope, type Dino-Lite Pro AM-413T (Dino-Lite Europe, Naarden, The Netherlands) with a 1.3 MP camera and a field of view of 1280 × 1024 pixels. The magnification was equal to 50, and the image resolution was approximately 6.8 μm per pixel. The 300 μm crack opening is a commonly applied limit presumably enabling an observable crack closure [38–41]. In addition, for comparison, three beams were kept intact in the water container as control samples until the end of the experiment. These series of samples were used for the water absorption rate test and crack closure observations.

Three mortar beams were cut into nine 4 × 4 × 4 cm cubes. Three of these cubes were subjected to a uniaxial compression test at 7 days to verify the maximum (100%) peak load. The uniaxial compression machine, type Instron, model 1342 (Instron, Norwood, United States), was used. Subsequently, after knowing the maximum peak load, additional three cubes were damaged to 80% of the peak load to induce cracks. For comparison, the remaining three undamaged cubes were kept in the water container until the end of the experiment. These series of samples were used for the compression strength recovery measurements. The cracking pattern induced by the compression test differed from the three-point bending test, with many narrow cracks formed within the specimen volume.

2.3.2. Self-healing exposure

After cracking, the specimens were immersed in tap water following a cyclic exposure with 3-day wetting and 3-day drying phase. Four cycles were applied, resulting in a total of 24 days of healing. The length of the cycle was determined with trial experiments. During the wetting phases, samples associated with the same binder composition were kept in the same sealed plastic container. All containers had a similar water level, fully covering the specimens. Afterward, the specimens were taken out of the water and kept at approximately 20 °C and 40% relative humidity. All samples were placed in the same room, with the crack opening directed upwards.

Water was exchanged between the cycles to enhance the calcium-leaching process by potentially increasing the ion concentration gradients to enable the ion transfer into the crack [42]. In addition, the cyclic exposure was considered more realistic regarding field conditions. For instance, it could be used on large-scale concrete elements by applying cyclic spraying.

2.3.3. Self-healing efficiency

The efficiency of self-healing was evaluated using microscopy, compressive strength recovery, and water absorption rate test. The self-healing at the crack mouth, i.e., external self-healing, related possibly to the calcite precipitation mechanism, was evaluated with a digital optical microscope. On the other hand, the strength recovery and water absorption rate test indirectly gave information regarding the healing of the crack deeper inside the specimen, i.e., the internal crack closure, associated primarily with the ongoing hydration mechanism.

Images of the cracked mortar beams were taken before and after the healing process. The resolution of the images was 1280 × 1024 pixels. A unique stand was prepared to maintain the same position during the image acquisition before and after healing (Fig. 3a). Four images per sample were obtained, covering approximately 32 mm of the crack length with different crack width intervals (Fig. 3b). In total, 360 images were analyzed, i.e., 180 images, before and after healing.

The crack closure was calculated using the Fiji image processing package [43]. First, the RGB images were converted to 8-bit grayscale and binarized with the Sauvola local thresholding algorithm [44], where white pixels (with value 1) represented an empty crack and black pixels (with value 0) the background (mortar matrix). As a result, crack closure CC was calculated as:

$$CC = \left(1 - \frac{\sum_{i=1}^{n} A_{h,i}}{\sum_{i=1}^{n} A_{0,i}}\right) * 100 [\%] \tag{1}$$

where $A_{0,i}$ and $A_{h,i}$ depict a sum of white pixels (empty crack area) in the image i of the crack before and after healing, respectively.

After four dry/wet healing cycles, the water absorption rate test was performed on three cracked and three undamaged mortar beams to determine the change in the water transport properties for each mix composition. A methodology similar to ASTM C1585 [45] standard procedure was adopted. This test measures the water uptake by determination of the capillary suction in specific time intervals [17]. Firstly, the specimens were dried in an oven at 55 °C until the weight change was less than 0.2%, and a silicone layer was applied on four sides of the beam [46]. Afterward, the beams were placed in a water container so that the bottom surface of the specimen was in contact with water. The water level was kept at approximately 4 mm above the bottom surface of
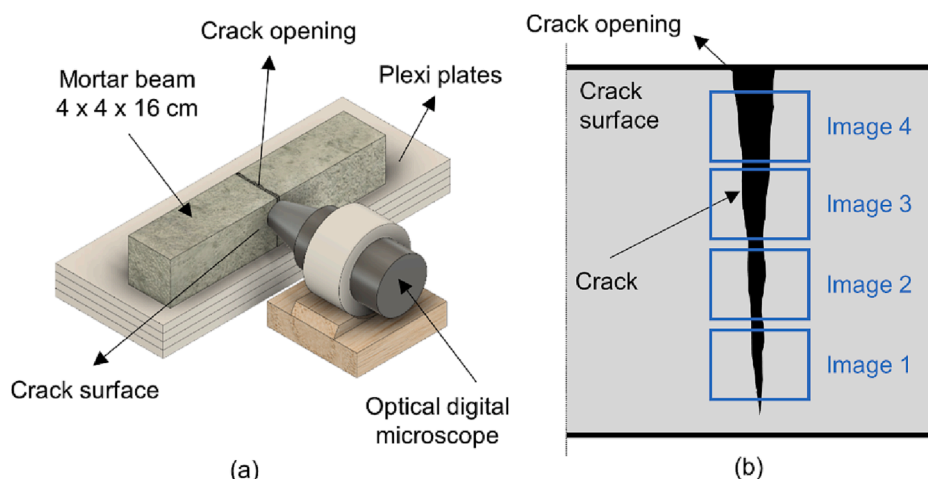

Fig. 3. Image acquisition setup: (a) microscope stand [4], (b) image positions on the crack surface.

the specimen (Fig. 4).

Change in the mass of the sample was recorded in the following time intervals: 0, 5, 15, 25, 45, 60, 120, and 180 min. Before weighing, the excess water was removed from the specimen with a cotton cloth. After each measurement, the samples were returned to the water [47]. The cumulative rate of water absorption I in each moment of time t is defined as:

$$I(t) = \frac{\Delta m}{A \bullet \rho} \, [mm] \tag{2}$$

where Δm is the change in mass of the sample (g), A is the area of the bottom surface (mm^2) and ρ is the density of water (g/mm^3). Two transport properties recovery parameters $IR25$ and $IR180$ were calculated based on the cumulative values of water absorption after 25 min (I_{25}) and 180 min (I_{180}):

$$IR25 = \frac{1}{n}\sum_{i=1}^{n} I^i_{25,h} - \frac{1}{n}\sum_{i=1}^{n} I^i_{25,un} \, [mm] \tag{3}$$

$$IR180 = \frac{1}{n}\sum_{i=1}^{n} I^i_{180,h} - \frac{1}{n}\sum_{i=1}^{n} I^i_{180,un} \, [mm] \tag{4}$$

where n is the total number of specimens, $I^i_{25,h}$ and $I^i_{25,un}$ are the values of cumulative water absorption at 25 min for healed and undamaged i-th specimen, respectively, and $I^i_{180,h}$ and $I^i_{180,un}$ are the values of cumulative water absorption at 180 min for healed and undamaged i-the specimen, respectively. Smaller values of $IR25$ and $IR180$ correspond to more successful healing.

The coefficient of sorptivity S_{25} of the specimens was determined as a slope of the absorption curve against the square root of time (min$^{1/2}$) [46,47]. Data during the initial 25 min were considered [17]. The sorptivity recovery parameter $SR25$ was calculated as follows:

$$SR25 = \frac{S_{25,h}}{S_{25,un}} \, [-] \tag{5}$$

where $S_{25,h}$ and $S_{25,un}$ are the slopes of the initial 25 min of the water absorption curves for healed and undamaged specimens, respectively. The smaller the value of SR25, the more effective the self-healing process could be assumed.

After four healing cycles, the compressive strength recovery was measured. Self-healing of two damage extents was evaluated, i.e., 80% and 100%, as described in Section 2.2.1. Three types of 4 cm × 4 cm × 4 cm cubes were tested: pre-loaded with 80% peak load, pre-loaded with 100% peak load, and undamaged cubes. The following compressive strength recovery parameters, $CSR80$ and $CSR100$, were determined:

$$CSR80 = \frac{\frac{1}{n}\sum_{i=1}^{n} S_{80,i}}{\frac{1}{n}\sum_{i=1}^{n} S_{un,i}} \, [-] \tag{6}$$

$$CSR100 = \frac{\frac{1}{n}\sum_{i=1}^{n} S_{100,i}}{\frac{1}{n}\sum_{i=1}^{n} S_{un,i}} \, [-] \tag{7}$$

where n is the number of cubes tested, S_{80} and S_{100} are the compressive strengths after 24 days of healing for specimens subjected to an 80% and 100% maximum peak load, respectively, and S_{un} depicts the reference compressive strength of undamaged cubes at age 7 + 24 days. The efficiency of the healing process is more significant for higher values of the CSR parameters.

2.3.4. Microstructure and chemical composition

The samples used for the Scanning Electron Microscope (SEM) were approximately 3 mm thick slices cut from the center of the sample. The hydration was stopped using an isopropanol solvent exchange method for 7 days, followed by vacuum drying in a desiccator for 48 h. A central slice piece was then impregnated under a vacuum with epoxy resin and polished using Struers CitoVac and Labosystem (Struers, Ballerup, Denmark). Struers MD Largo discs and DP-Spray M diamond suspensions with decreasing particle sizes were applied. Firstly, the 9 μm particle suspension was used with the 20 N pressure for 30 min, followed by 2 h with the 3 μm suspension at 25 N and 3 h with the 1 μm suspension at 25 N. Paraffin-based lamp oil was used as a lubricant. To remove the remaining suspension, the specimens were rinsed in an isopropanol-filled ultrasonic bath between each step [48]. After polishing, all samples were vacuum-dried in the desiccator for 48 h before the SEM analysis.

For X-ray Diffraction (XRD), approximately 3 g of a hardened paste was crushed with mortar and pestle to pass a 1 mm aperture sieve. The hydration of Portland cement was hindered by the isopropanol solvent exchange method following the RILEM TC-238 recommendation [49]. The powder was immersed in 100 ml of isopropanol for 15 min, vacuum filtered on the Büchner filter, and dried for approximately 8 min in an oven at 40 °C.

A Jeol JSM-IT100 scanning electron microscope (SEM) (JEOL Ltd., Tokyo, Japan) with a Bruker energy-dispersive X-ray spectroscope (EDX) (Bruker Corporation, Billerica, MA, USA) was used for the microstructural analysis. To prevent charging, the backscatter electron (BE) mode was used at a low vacuum with the pressure set to 30 Pa, the accelerating voltage was 15 kV, and the working distance was 12 ± 1 mm.

The porosity of the cement paste was calculated based on the obtained BE images according to the overflow method [50]. Greyscale images were acquired at 400x magnification in thirty locations per sample (Fig. 5a). Each image was binarised 51 times (every 5 grey scale values) to obtain the cumulative curve (Fig. 5b) of the segmented area. The Fiji image processing package [43] with ImageJ2 software [51,52] was used for image processing. The so-called "critical overflow point," being the final threshold, was determined in OriginPro software (v. 2020, OriginLab Corporation, Northampton, Massachusetts, USA) by estimating the inflection of the cumulative curve from the intersection of
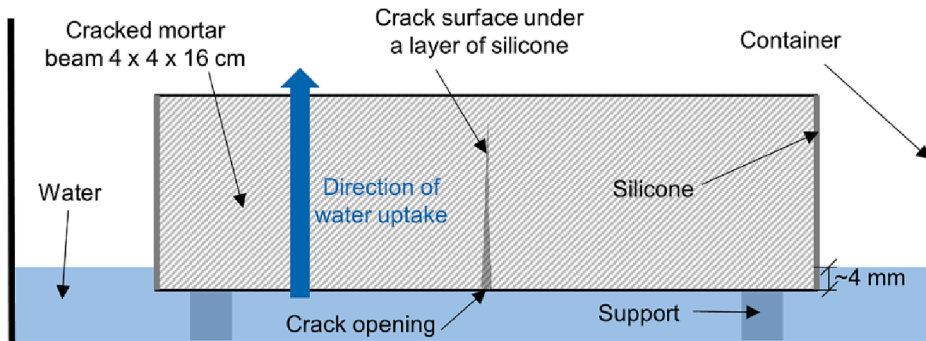

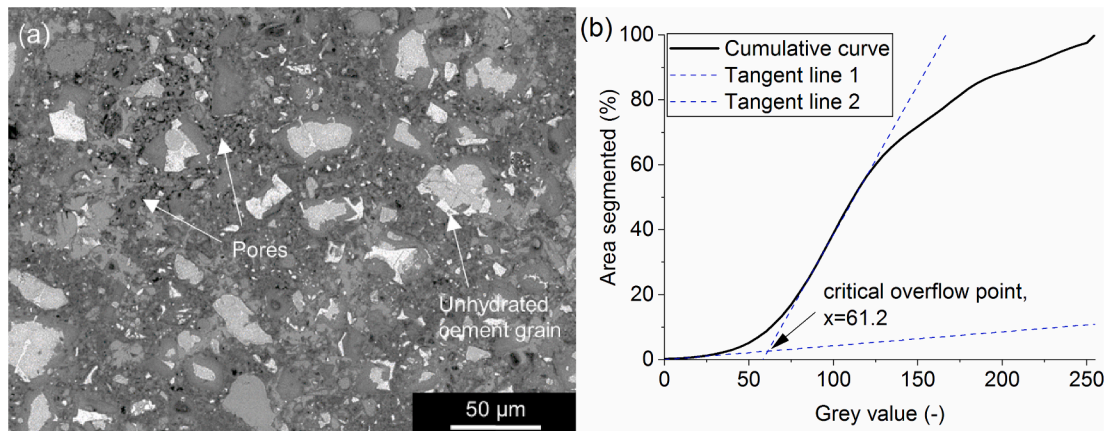**Fig. 4.** Water absorption rate test setup.

Fig. 5. (a) Example of SEM image (BE 400x) for porosity analysis; (b) Porosity threshold estimation from cumulative curve;

two tangent lines (Fig. 5b). The final threshold for each image was set as the × coordinate of the intersection point (e.g., x = 61.2 in Fig. 5b). The images were then binarised, and the mean porosity μ_p was calculated as follows:

$$\mu_p = \frac{1}{n}\sum_1^n \left(\frac{X_i}{Y_i} \bullet 100\right)[\%] \tag{8}$$

where X_i and Y_i are the area fractions of pores and cement matrix for image i, and n represents the total number of images.

The composition of the inner product (IP) C–A–S–H was determined using SEM-EDX with Bruker Esprit software (version 2.1). Guidelines from [53] were applied. In total, 100 points were analyzed (10 points in 10 different locations) per sample at 4000× magnification. The points were chosen manually within the IP C–A–S–H (Fig. 6a). The same number of X-rays per acquisition (50,000 counts per analysis) was maintained, resulting in a total acquisition time of approximately 7 min per location. The average IP C–A–S–H composition, i.e., the atomic ratio of Si/Ca, was determined by applying the so-called Edge of the Cloud of Points approach [53]. Gaussian distribution was fitted to the histograms of the raw data (100 points, histogram binning 0.01) for each specimen (Fig. 6b). The average Si/Ca ratio was calculated as follows:

$$\frac{\text{Si}}{\text{Ca}} = \mu + 2\sigma[-] \tag{9}$$

where μ and σ are the mean value and standard deviation of the fitted distribution, respectively (Fig. 6b).

An X-ray diffractometer type Empyrean from PANalytical with

PIXcel 3D detector (Malvern Panalytical Ltd., Royston, UK) was used to verify the chemical composition of the hardened paste. Cu-K radiation with a wavelength of 1.54060 Å was applied, which was generated at 45 kV and 40 mA. The step size was 0.0260, and the angle range of 2θ was from 5° to 65° resulting in approximately 15 min acquisition time per analysis. Panalytical's Highscore Plus software, equipped with a COD database, was used to determine the phase composition. A semi-quantitative analysis was performed using OriginPro's Quick Peak tool by computing the approximate area of the first peak of the Portlandite and calcium carbonate phases. The baseline was subtracted, and the peak area was calculated by integrating the raw data from the baseline. The full width at a half-maximum height (FWHM) was also verified.

2.3.5. Crack complexity

The initial pre-healing geometry of the cracks was characterized by the following parameters calculated based on the crack images before healing: initial crack area (ICA), maximum crack width (MCW), average crack width (ACW), tortuosity (T) and fractal dimension (FD). The Fiji image processing package was also used for this analysis [43].

The initial crack area (ICA) was defined as a sum of white pixels corresponding to the crack area. To calculate the width of the crack (MCW and ACW), a local thickness definition $\tau(\overrightarrow{p})$ was used as proposed by [54], i.e., a diameter of the largest sphere that fits inside the object and contains a given point (Fig. 7a):

$$\tau(\overrightarrow{p}) = 2\max(\{r|\overrightarrow{p} \in sph(\overrightarrow{x}, r) \subseteq \Omega, \overrightarrow{x} \in \Omega\}) \tag{10}$$

where Ω is the set of all points in the spatial structure, $\overrightarrow{p}$ is an arbitrary
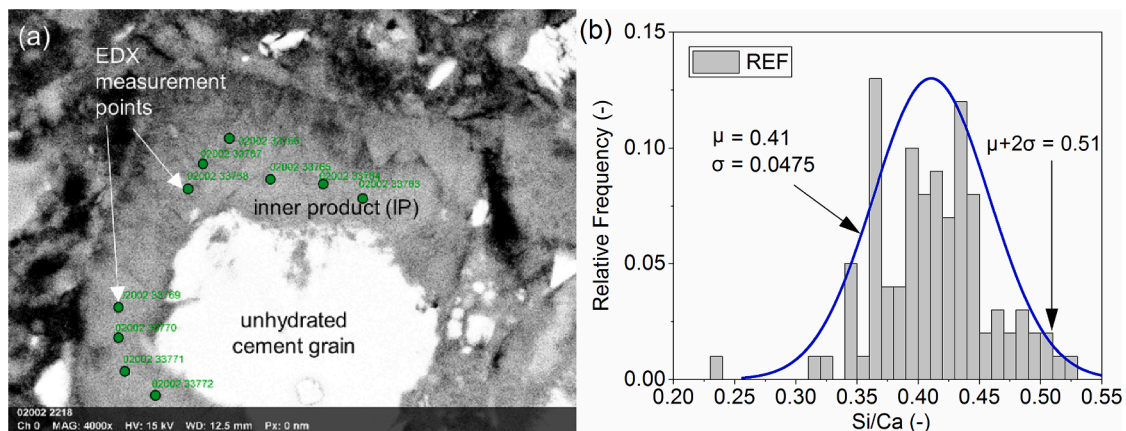

Fig. 6. (a) 4000x BSE-SEM image of a polished section with marked 10 EDX measurement points in the inner product (IP) C–A–S–H in one location; (b) fitting procedure for IP C–A–S–H Si/Ca ratio based on (Rossen and Skrivener, 2017).
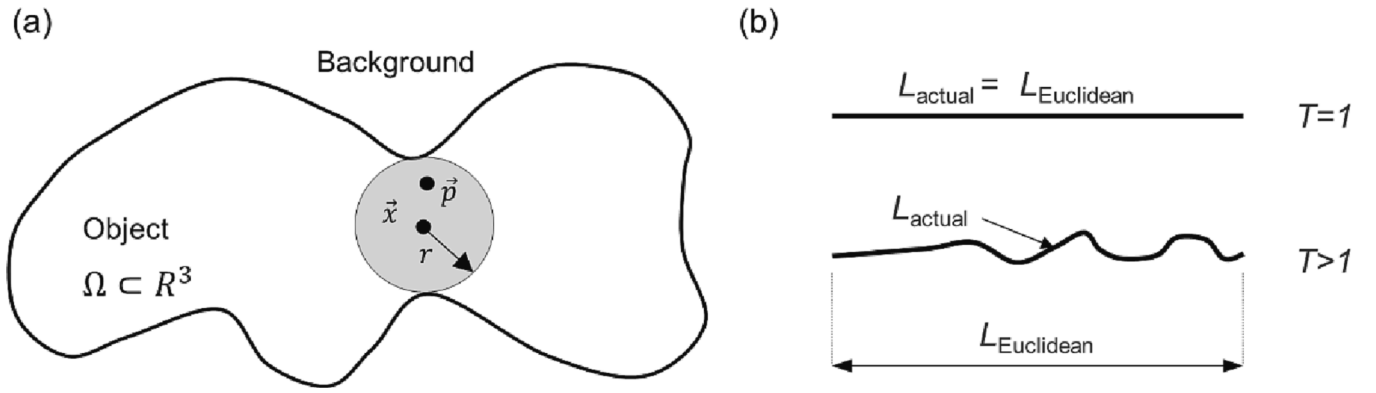
Fig. 7. Schematic definition: (a) local thickness, (b) tortuosity.

point in the structure, $sph(\vec{x}, r)$ is the set of points inside a sphere characterized by a center $\vec{x}$ and a radius r [54]. The local thickness plugin in the Fiji package was used for the calculation [55].

Also, the 32-bit local thickness maps were generated (Fig. 8a1), where each pixel value was equal to the thickness of a crack at a given point. Based on the maps, the histograms of the local thickness distribution were created (Fig. 8a2). The maximum value of the crack thickness was assumed as MCW. Finally, an average crack width (ACW) was calculated as a weighted average from the histogram following the

equation (11):

$$\text{ACW} = \frac{\sum_{i=1}^{n} c_i \tau_i}{\sum_{i=1}^{n} c_i} [\mu m] \qquad (11)$$

where n is the number of bins, c_i is the number of counts per each thickness τ_i.

The crack tortuosity (T) describes the curvature of the crack profile (Fig. 7b). It is defined as the difference between the actual crack length
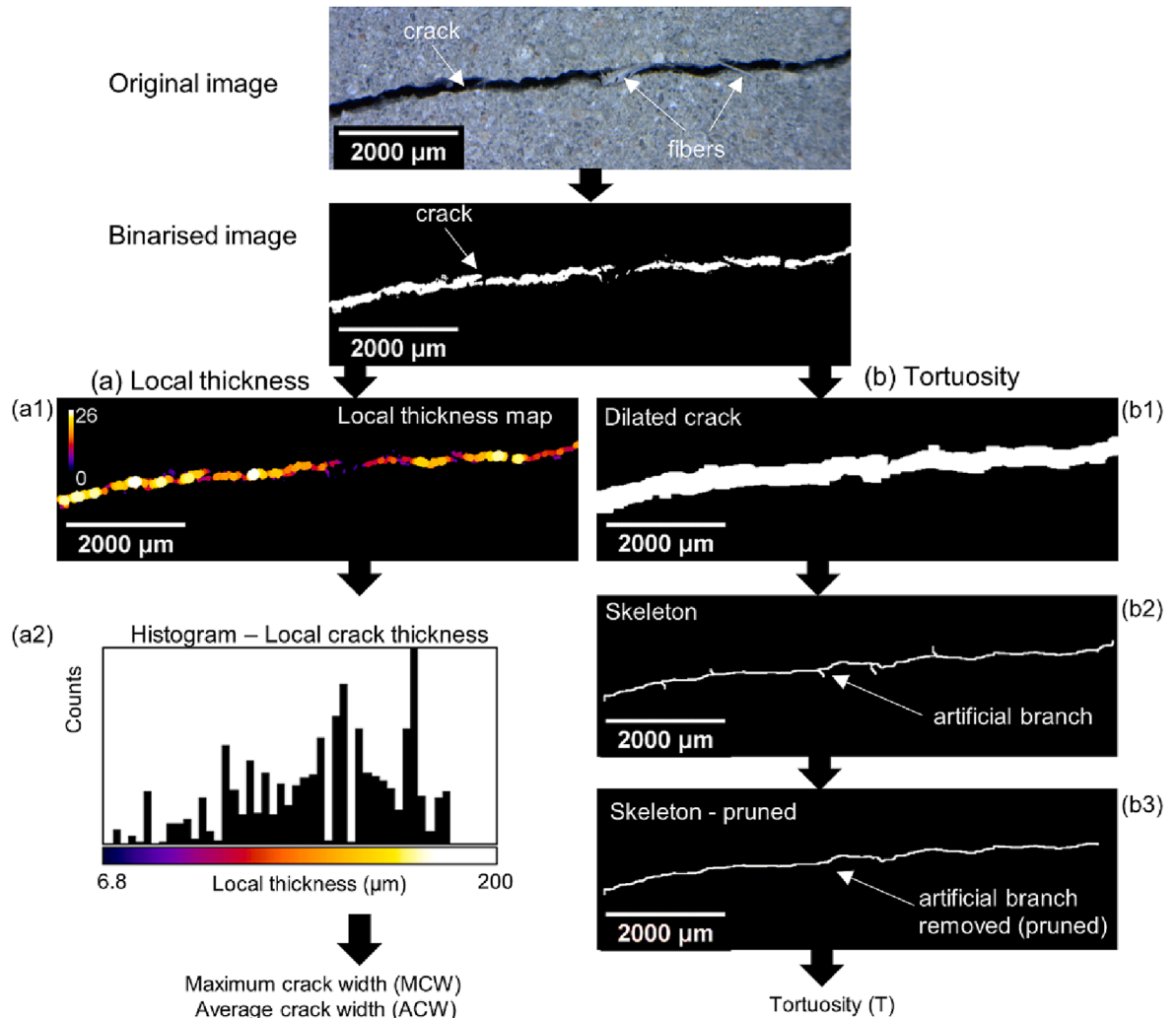

Fig. 8. The image processing procedure for the (a1-a2) calculation of maximum crack width (MCW), average crack width (ACW), and (b1-b3) tortuosity (T).

and the Euclidean distance [56]:

$$T = \frac{L_{actual}}{L_{Euclidean}} \; [-] \tag{12}$$

where L_{actual} is the effective length of the crack and $L_{Euclidean}$ is the shortest distance between the start and end point of the crack in Euclidean space. The crack tortuosity calculation required preprocessing of the binarised images (Fig. 8b1-b3) due to many crack discontinuities resulting from the presence of the fibers inside the crack. The dilation procedure was used to merge parts of the crack (Fig. 8b1). Afterward, the "skeletonization" algorithm was applied [57,58]; with the use of the Skeletonize(2D/3D) plugin available in the Fiji package to distinguish the crack profile (skeleton, Fig. 8b2). The skeleton was then pruned by removing the artificially created crack branches shorter than 70 pixels (Fig. 8b3). To estimate L_{actual} and $L_{Euclidean}$, the crack profile measurements were performed using the Analyze Skeleton(2D/3D) Fiji plugin.

Fractal dimension (FD) is a parameter used to characterize the complexity of structures, i.e., the change of the pattern detail with the change in scale. It describes the degree of filling of a metric space by the analyzed object, e.g., for a curve, it can be equal between 1 and 2 [27]. Among several methods that allow determining the FD, the box-counting method is the most frequently used due to its simplicity [59]. In this method, a series of grids (boxes) of descending sizes is positioned over an image. For each grid, the number of boxes intersecting the object and the box size are counted [60]. The fractal dimension for the box-counting method (FD) is determined as:

$$FD = \lim_{\varepsilon \to \infty} \frac{\log N_{\varepsilon}}{\log \varepsilon} \tag{13}$$

where N_{ε} is the number of boxes that contain pixels of the analyzed object, ε denotes the scale applied to the object, i.e., box size relative to the image size. In practice, the limit is the slope of the regression line of the log–log plot of the data.

In this paper, the fractal dimension of the cracks was calculated using the box-counting method in FracLac for ImageJ [61]. Linear grid sampling size (box size) was used, with the largest element size limited to 45% length of the shorter edge of the image. Twelve different grid orientations were measured to facilitate a more efficient covering of the crack structure. The fractal dimension was calculated as the slope of the regression line of the $\ln N_{\varepsilon}$-$\ln \varepsilon$ plot for each grid position, and an average value from twelve measurements was assumed.

3. Results and discussion

3.1. Initial microstructure and phase composition

XRD patterns of the initial microstructure of the investigated cementitious materials are presented in Fig. 9. Peaks corresponding to the portlandite phases are marked with the letter P, and calcium carbonate phases with the letter C. An increased amount of calcium in the microstructure could presumably lead to its intensified dissolution and reaction with water inside the crack during the healing process leading to the formation of additional calcium carbonate and C-S-H phases
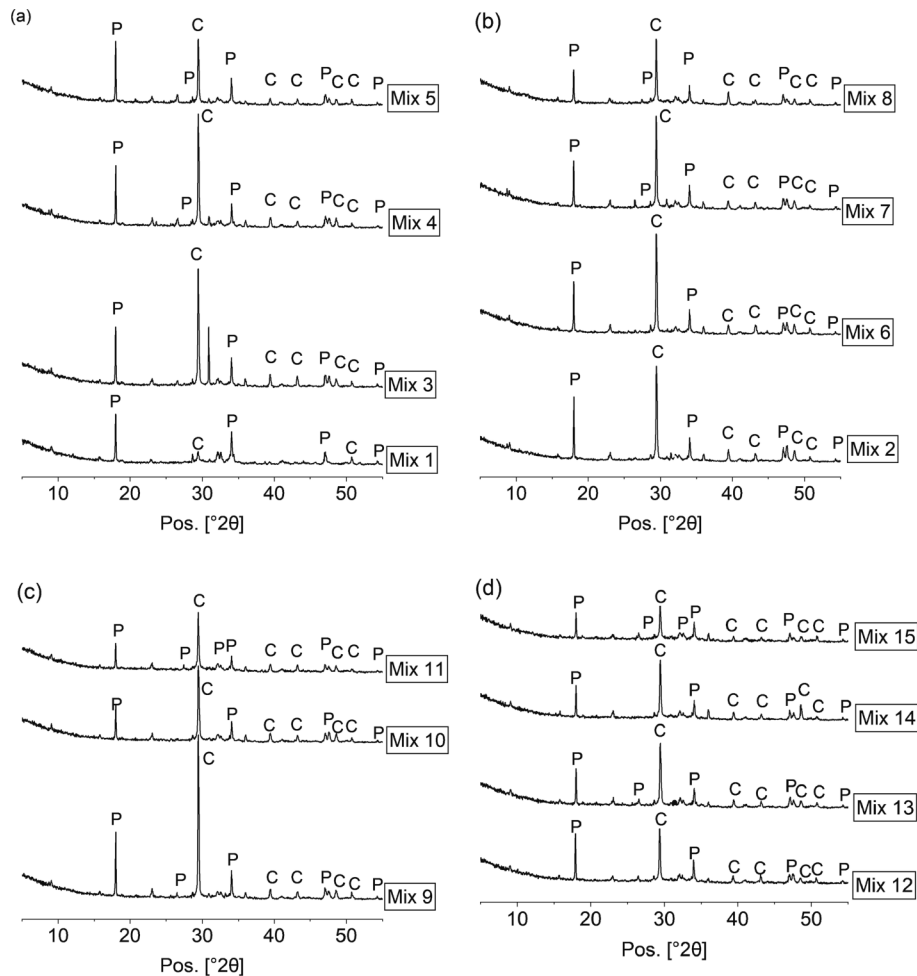

Fig. 9. XRD patterns with marked Portlandite (P) and calcium carbonate (C) phases.

inside the crack. It is visible that with different SCM/limestone ratios, peak intensities of C and P vary due to chemical reactions between the constituents (Fig. 9). To allow a semi-quantitative comparison of the amounts of portlandite and calcium carbonate phases, the area under the first peak of each phase was calculated (Table 3).

Cementitious composites with LM and FA (Mixes 3–5) show an invariable amount of Portlandite (Table 3, Fig. 10), equal to approximately 87, which is relatively higher than in the case of other mixes with SCMs. However, a relatively significant decrease in the amount of Portlandite is visible with the increasing amount of S (Mixes 6–8) and SF (Mixes 9–11) (Table 3, Fig. 10). It could suggest a considerably lower FA reactivity than S and SF, which is also connected to the early age of the cementitious materials, i.e., 7 days. In addition, a factor negatively affecting the portlandite reaction could be the limited transport within a dense binder matrix [11]. As seen from the porosity results (Fig. 12), the lowest porosity was achieved for the fly ash systems suggesting that the reaction of Portlandite could be restricted. As anticipated, calcium carbonate phases, associated primarily with the limestone content, are decreasing with the increasing ratio of replacement with SCMs, reaching the lowest values for quaternary binders (Mixes 12–15). The decrease may also be caused by the calcite consumption in these binder mixes [11].

Changes in the chemical composition of the C–A–S–H gel were evaluated based on the Si/Ca ratio (Table 4, Fig. 11) of the homogenous "inner products" (IP C–A–S–H). Negligible differences were observed for most cementitious composites, with the calculated Si/Ca values ranging between 0.5 and 0.6. However, noticeably higher Si/Ca ratios were measured for the mixes with a higher dosage of silica fume and fly ash (Mixes 5, 11, and 15), with the Si/Ca ratio between 0.6 and 0.72.

Binder composition had an evident impact on the porosity (Table 4, Fig. 12). Composites with a large amount of silica fume and slag were characterized by relatively high porosity. Conversely, fly ash, and pure limestone mixes showed low porosity.

3.2. Crack complexity

The crack complexity parameters were evaluated based on the images obtained for each of the four microscope positions, as shown in Fig. 3b. For each position, the average and maximum crack widths were

Table 3
Calculated peak areas for semi-quantitative comparison of Portlandite and calcium carbonate.

| #	Mix	Portlandite at approx. $2\theta = 18°$		Calcium carbonate at approx. $2\theta = 29°$	
		Peak Area (–)	FWHM (–)	Peak Area (–)	FWHM (–)
Mix 1	REF	78.001	0.123	22.806	0.199
Mix 2	LM50	82.546	0.103	230.526	0.188
Mix 3	LM43.75 FA6.25	86.041	0.113	285.189	0.182
Mix 4	LM37.5 FA12.5	87.740	0.108	251.088	0.177
Mix 5	LM25 FA25	88.863	0.111	153.797	0.185
Mix 6	LM43.75 S6.25	75.843	0.115	241.069	0.187
Mix 7	LM37.5 S12.5	68.424	0.107	196.889	0.168
Mix 8	LM25 S25	51.268	0.116	137.819	0.159
Mix 9	LM43.75 SF6.25	93.414	0.106	370.029	0.173
Mix 10	LM37.5 SF12.5	55.699	0.113	201.401	0.206
Mix 11	LM25 SF25	37.819	0.115	137.511	0.175
Mix 12	LM25 FA12.5 S12.5	73.534	0.124	124.986	0.190
Mix 13	LM25 FA12.5 SF12.5	52.063	0.119	164.117	0.214
Mix 14	LM25 S12.5 SF12.5	45.042	0.104	153.214	0.194
Mix 15	LM12.5 FA12.5 S12.5 SF12.5	35.681	0.109	81.325	0.183
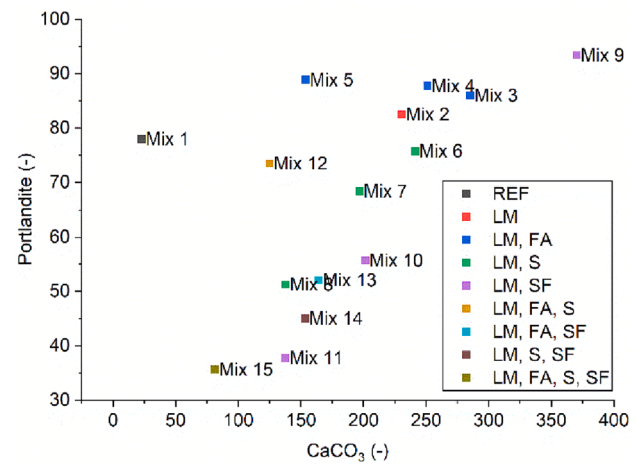
Fig. 10. Semi-quantitative analysis of Portlandite and CaCO$_3$ for different binders.

calculated using the local thickness algorithm, as described in Section 2; in total, 45 images per position. The following approximate values of the maximum crack widths per position were obtained: 100 μm, 130 μm, 170 μm, and 190 μm. On the other hand, the average crack widths were equal to around: 65 μm, 80 μm, 95 μm, and 105 μm per position. Fig. 13 demonstrates tortuosity (Fig. 13a) and fractal dimension (Fig. 13b) with marked significant differences for pairwise comparison verified using Tukey's range test. No relation between the crack tortuosity and the average crack width was detected. Based on the calculated fractal dimensions, it was concluded that a more complex cracking pattern was observed with increasing average crack widths (Fig. 13b).

Minor differences between the average values of the crack complexity parameters were observed concerning the binder composition. The average tortuosity was between 1.1 and 1.13 (Fig. 14a), whereas the fractal dimension (FD) for all the cementitious materials was between 1.26 and 1.37 (Fig. 14b). The limited variation of the results can be justified by the characteristics of the three-point bending test used to produce cracks and the lack of coarse aggregate. The three-point bending test formed reasonably linear cracks with a relatively low complexity level.

3.3. Self-healing efficiency
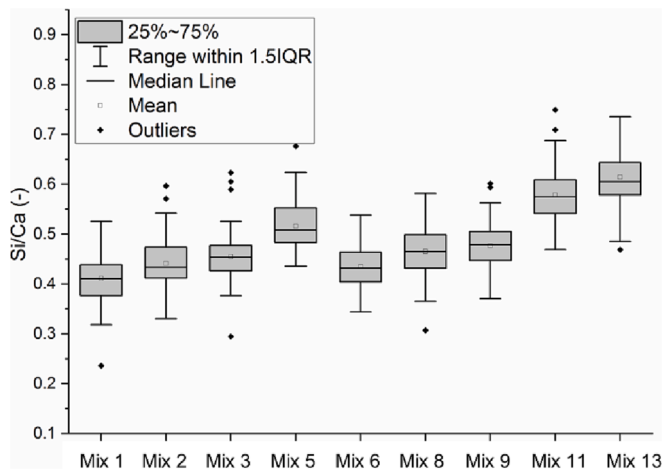
3.3.1. Crack closure

The images of the cracked surface for selected specimens are shown in Fig. 15. Self-healing products are noticeable in the crack mouth. The morphology of the self-healing material, i.e., microscopic white crystals, suggests possible calcium carbonate precipitates. As anticipated, no preferential precipitation was observed around the PP fibers.

The quantitative estimation of crack closure (CC) indicated more pronounced healing for the maximum crack widths below 130 μm for all mixes (Fig. 16a–f). The highest external crack closure, approximately 50–60%, was achieved for the mixes with higher slag amounts: LM37.5 S12.5 (Mix 7) and LM25 S25 (Mix 8) (Fig. 16c). Ternary and quaternary binders (Fig. 16ef) with varying slag content, LM25 FA12.5 S12.5 (Mix 12), LM25 S12.5 SF12.5 (Mix 14) and LM12.5 FA12.5 S12.5 SF12.5 (Mix 15) also exhibited a relatively high crack closure index compared with the reference mix (Mix 1, 100% OPC). Mix 2, with only Portland cement and limestone (LM50), showed an improved crack closure compared to the reference mix (Fig. 16a). The replacement of limestone with fly ash (Mixes 3–5) decreased the external crack closure (Fig. 16b). The decreased crack closure could be associated with the low reactivity of the type F fly ash due to the small amount of CaO available [22]. A moderate amount of silica fume (up to 12.5 wt%, Mixes 9 and 10) gave a similar crack closure ratio as pure limestone mix (Mix 2, LM50);

Table 4

Calculated IP C–A–S–H composition (Si/Ca) and porosity values (Std – standard deviation).

#	Mix	IP C–A–S–H composition				Porosity		
		Number of points (−)	Mean (−)	Std (−)	Calculated Si/Ca (−)	Number of images	Mean (%)	Std (%)
Mix 1	REF	100	0.41	0.048	0.51	31	8.90	0.57
Mix 2	LM50	100	0.44	0.048	0.54	29	3.53	0.83
Mix 3	LM43.75 FA6.25	100	0.46	0.045	0.55	30	3.09	0.83
Mix 5	LM25 FA25	100	0.52	0.044	0.60	30	3.47	0.90
Mix 6	LM43.75 S6.25	100	0.44	0.040	0.52	30	3.77	0.95
Mix 8	LM25 S25	100	0.47	0.049	0.56	30	6.58	0.94
Mix 9	LM43.75 SF6.25	100	0.48	0.040	0.56	30	3.02	1.07
Mix 11	LM25 SF25	100	0.58	0.049	0.68	30	14.77	2.33
Mix 15	LM12.5 FA12.5 S12.5 SF12.5	100	0.61	0.052	0.72	30	14.27	2.45

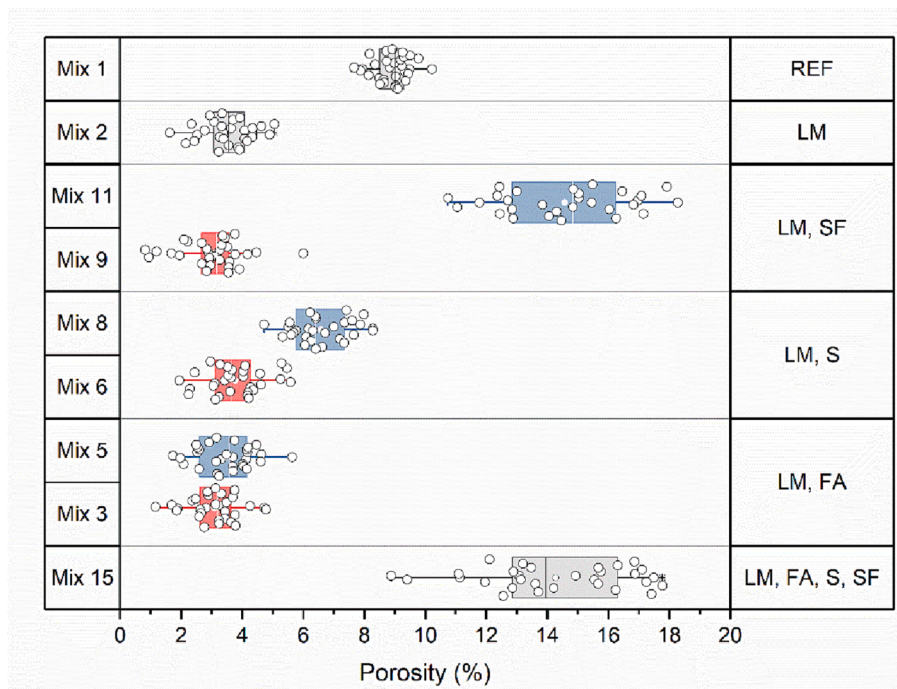**Fig. 11.** Effect of the mix composition on the IP C–A–S–H Si/Ca ratio.

however, the addition of 25 wt% of silica fume (Mix 11) had a detrimental effect on the healing of the crack.

Relatively limited crack closure, with maximum CC reaching approximately 60%, could be presumably linked to the cyclic healing exposure. A more extended wetting phase or a complete water immersion could possibly increase the external crack sealing ratio [18].

3.3.2. Strength regains

Compressive strength results are listed in Table 5. All values were measured at 7 + 24 days. The values for undamaged specimens S_{un} correspond approximately to the 28 days strength. A high cement replacement resulted in a compressive strength decrease in comparison to the REF mix (Mix 1, 100 %OPC). Nevertheless, all mixes reached a compressive strength above 20 MPa.

The highest strength regain was achieved for the low amount of fly ash (Mix 3, LM43.75 FA6.25), Fig. 17ab. Conversely, the higher the fly ash/limestone ratio, the lower regain of the strength was observed (Fig. 18a and 19a). An opposite trend was visible for samples containing slag (Mixes 6–8). The higher the slag/limestone ratio, the better the strength recovery ratio (Fig. 18b and 19b), especially for the lower damage (CSR80, Fig. 18b). Adding silica fume (Mixes 9–11) also positively affected the healing considering compressive strength recovery,

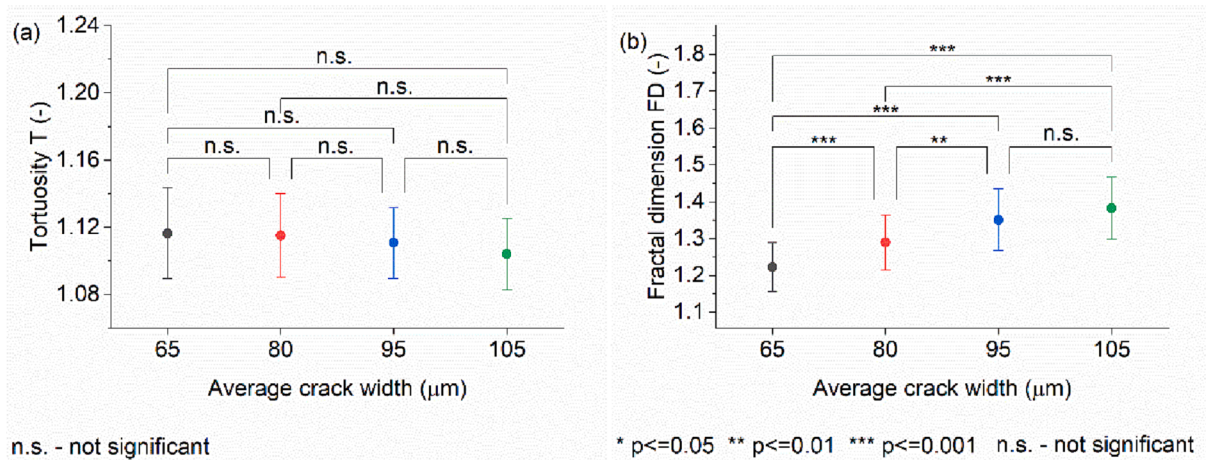**Fig. 12.** Effect of the mix composition on the porosity of the paste.

Fig. 13. Crack complexity parameters for different crack thickness ranges: (a) tortuosity (T), (b) fractal dimension (FD).
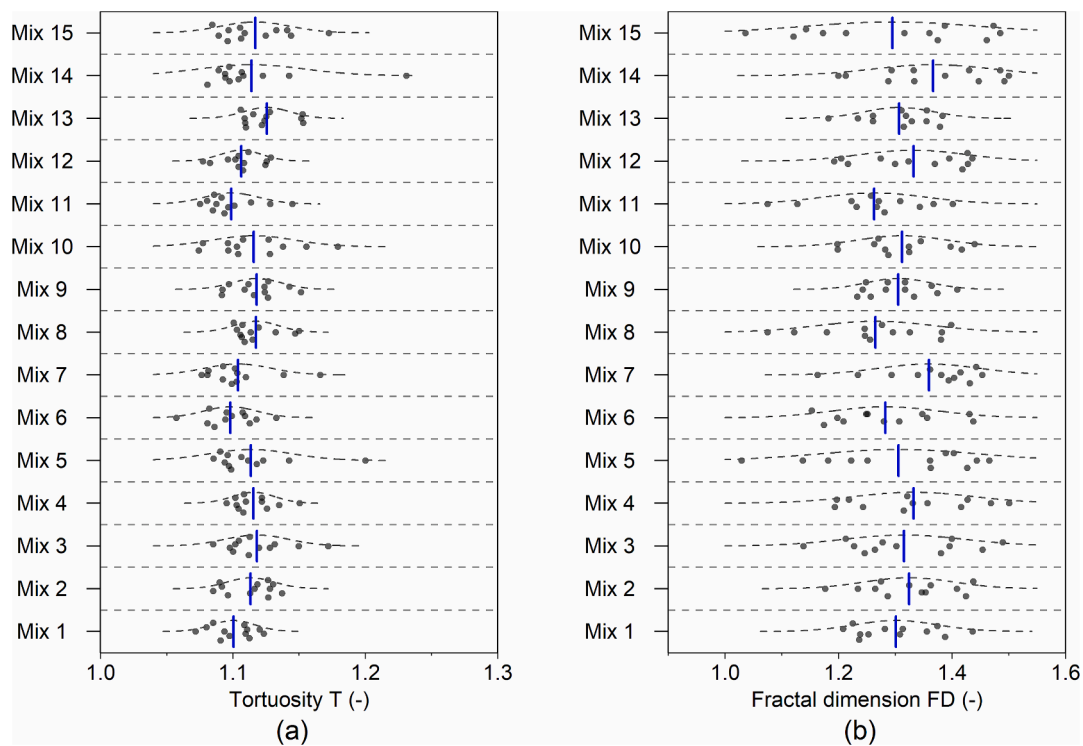

Fig. 14. Complexity parameters of the cracks for each mix (scatter with mean line and normal distribution): (a) tortuosity (T), (b) fractal dimension (FD).

with similar values achieved for all replacement levels (Figs. 17ab, 18c, and 19c).

In general, lower values of compressive strength regain were obtained concerning the higher degree of damage, with CSR100 between approximately 0.5–1.0, compared to 80% degree damage, with CSR80 equal to around 1.1–2.0 (Fig. 17).

Values of CSR parameters greater than 1 indicate that the compressive strength after healing was higher than the compressive strength of the intact specimen. CSR was defined as the relation between the healed and undamaged performance, measured on the same day, i.e., 7 + 24 days (age of cracking plus the duration of the healing process). The objective was to avoid bias associated with the early age of the samples when the cracks were induced, which is especially important concerning blended systems with low reactivity [62].

Nevertheless, despite the same age of the specimens, the early cracking could presumably affect the final values of compressive

strength. For example, in the case of F-type fly ash, its low reactivity causes slow hydration with up to 90 days required to obtain 28-day strength [63], which can be particularly significant for high replacement levels, i.e., Mix 5 (LM25 FA25). Low hydration degree at cracking presumably resulted in a large amount of unhydrated material exposed in the cracks. The microcracks formed by the compression test could facilitate water transport to the unhydrated particles, possibly accelerating the hydration reactions compared to the uncracked specimens and promoting self-healing. This agrees with other studies [64], which showed that dry/wet cycles promoted compressive strength increase for blended cementitious materials containing fly ash, slag, and silica fume. On the other hand, a detrimental effect of high amounts of fly ash (Mixes 4 and 5) on the strength recovery could also be associated with insufficient $Ca(OH)_2$ to enable the pozzolanic reaction.

Furthermore, the damage degree possibly impacted the self-healing process due to differences in crack widths formed during compression
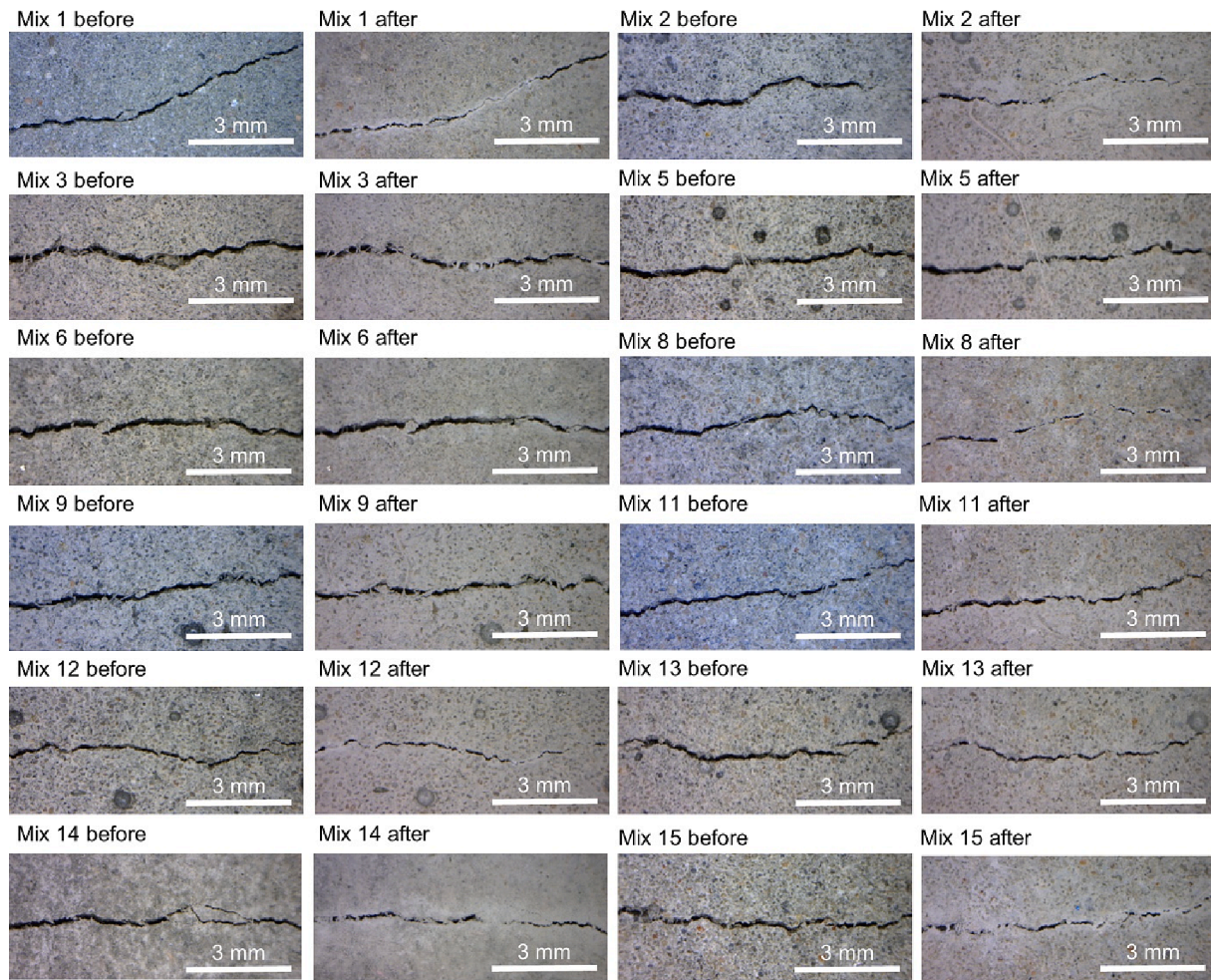
Fig. 15. Images of the cracks before and after self-healing for selected mix compositions.

at pre-loading rates of 80% and 100%. The sealing of finer cracks was less challenging than wider cracks resulting in higher mechanical performance regain for 80% damage (Fig. 17ab) for all specimens, which is consistent with the literature. For instance, it was observed that there is a particular damage threshold for self-healing efficiency [65]. The compressive strength regain was observed to increase with the increasing degree of damage, below the threshold value, reaching values above 1 in some instances. Conversely, above the threshold, mechanical performance recovery decreased with the increasing damage degree [65]. Therefore, it can be presumed that in the case of this study, the compressive strength recovery is a combination of reactions occurring within the immature binder matrix and the sealing of the formed microcracks.

Finally, it should be noted that the healed specimen's strength demonstrated a significant scatter (Table 5), on average between ± 5 and ± 7 MPa, which could be caused by an immature microstructure and diverse microcracking spatial distribution within the specimen volume. Nevertheless, it can be seen that for 100% damage (CSR100), the values of strength recovery are higher than the reference (Mix 1) for the majority of limestone-SCM blended binders.

3.3.3. Transport properties recovery

Transport properties recovery was evaluated based on the water absorption rate test. The determined absorption curves are presented in Fig. 20a-d, where the values correspond to an average of three measurements. Healed ("h") and intact (undamaged, "un") beams were tested on the same day, i.e., 7 + 24 days. In Fig. 21, cumulative water absorption change parameters at 25 min (IR25) and 180 min (IR180)

(Fig. 21a), and sorption coefficient (Fig. 21b) change for the first 25 min (SR25) are shown.

The most efficient healing related to the total water absorbed by the samples was observed for specimens with a high percentage of slag and silica fume, LM 25 S25 (Mix 8, Fig. 20c and 21a) and LM 25 S25 (Mix 11, Fig. 20d and 21a). Especially for a high amount of slag (LM 25 S25, Mix 8), both the water absorption (IR25/180, Fig. 21a) and the sorptivity (SR25, Fig. 21b) recovery parameters are close to 1, indicating that the healed material's behavior reached the state resembling the undamaged samples. Mix 8 was also twice as efficient as the reference (Mix 1, 100 % OPC) specimens.

Analogously as in the case of strength recovery, the increase in the amount of fly ash resulted in decreased healing, i.e., the parameters IR25, IR180, and SR25 have higher values for Mix 5 (LM25 FA25) than Mix 3 (LM43.75 FA6.25). On the contrary, the increase in the silica fume and slag has a positive effect on healing, which is also in good agreement with the compressive strength results.

A noticeable higher error in the case of some mixes, e.g., Mix 2 (LM50), could be caused by differences in crack geometry deeper inside the specimen or various spatial distributions of the PP fibers inside the crack, which could block water transport (Fig. 22a).

The water absorption rate test (Fig. 21) and compressive strength recovery (Fig. 17) indicated a higher self-healing efficiency despite a relatively low crack closure measured at the crack opening (Fig. 16). Others made similar observations, e.g. [18], for early-age cracked blended cementitious materials healed in wet/dry cycles as opposed to the continuous water immersion, where this effect was not present. It could be speculated that the self-healing phases were formed inside the
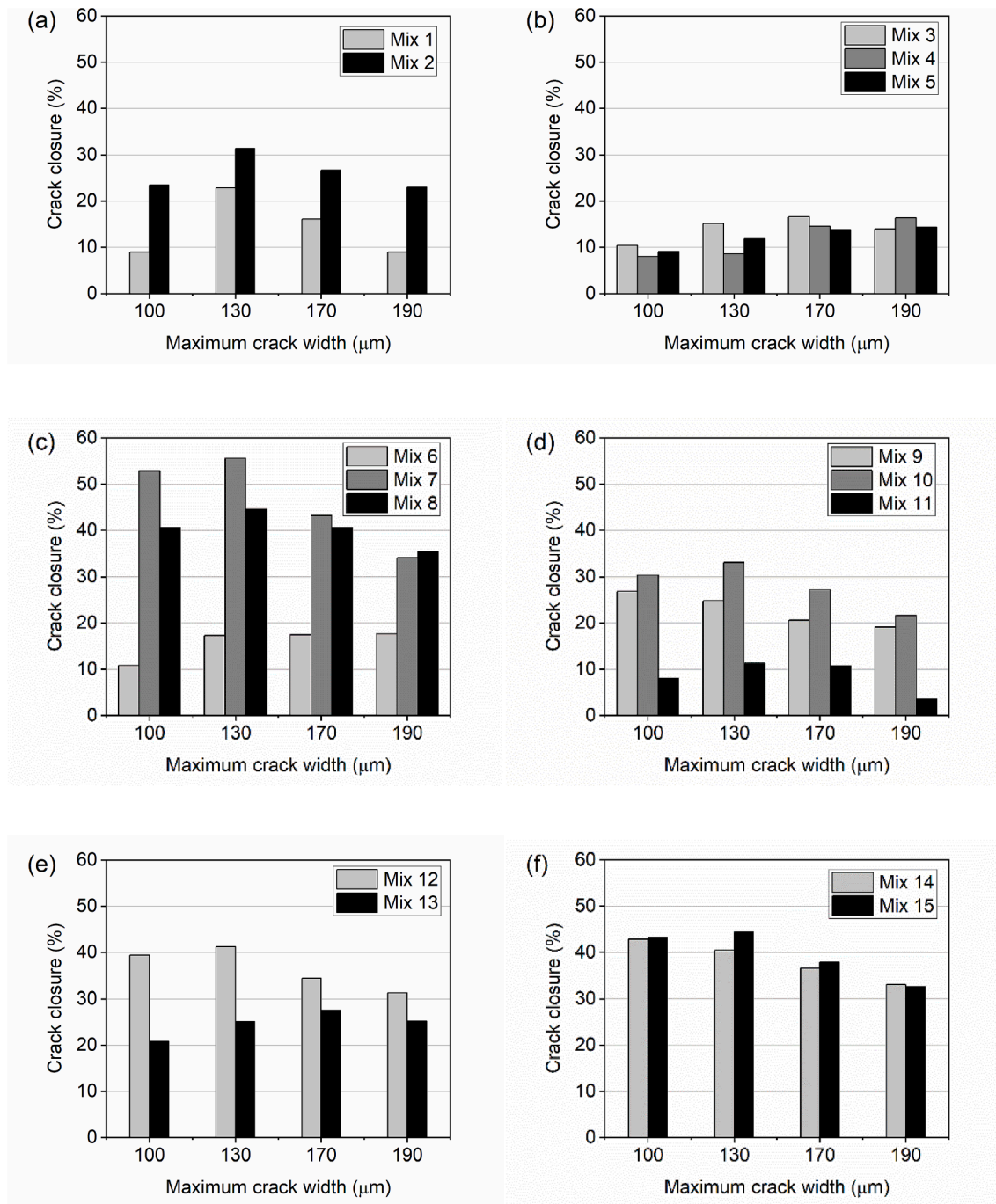
Fig. 16. Crack closure (CC) for mixes: (a) Mixes 1 and 2, (b) Mixes 3–5, (c) Mixes 6–8, (d) Mixes 9–11, (e) Mixes 12 and 13, (f) Mixes 14 and 15.

crack at depth (Fig. 22bc), which made them invisible for the optical microscope observations. Formation of the self-healing phases deeper inside the crack could be linked with the calcite precipitation or ongoing hydration mechanism. Differences in crack geometry at depth led to locally narrower cracks which facilitated self-healing product growth and local sealing of the crack, which contributed to decreased water absorption and increased strength recovery [39]. In addition, the ion concentration inside the crack varies with depth leading to a diverse spatial arrangement of the self-healing phases. For instance, load-bearing phases, such as C-S-H, could be formed deeper, promoting strength recovery [10]. Nevertheless, further studies should be conducted to confirm internal self-healing mechanisms, e.g., using X-ray microtomography or SEM cross-sections.

Furthermore, it should be noted that, in this study, the water

absorption test and compressive strength recovery compared the healed and intact specimens. The comparison with the damaged state was excluded from the investigation since the initial trials with the cracked specimens showed inconclusive results, possibly due to relatively low overall self-healing performance. A similar approach was applied in other studies, e.g., [66]) or [47]. In addition, a low variation in the average crack geometry parameters between different mixes (Fig. 13suggests that the damage was similar for all specimens; therefore, it could be assumed that the comparison with the intact state gave a good indication regarding the self-healing performance.

Table 5
Compressive strength results.

#	Compressive strength, undamaged S_{un} (MPa)		Compressive strength, 80 %damage, after healing S_{80} (MPa)		Compressive strength, 100% damage after healing S_{100} (MPa)	
	Mean value	Standard deviation	Mean value	Standard deviation	Mean value	Standard deviation
Mix 1	71.7	4.5	83.1	4.2	38.5	11.5
Mix 2	22.3	4.2	29.4	7.8	18.8	5.0
Mix 3	19.8	0.6	38.1	3.5	28.8	5.3
Mix 4	24.6	7.2	29.6	4.2	21.0	5.5
Mix 5	29.4	1.7	32.1	1.4	16.7	5.9
Mix 6	22.9	2.5	21.7	11.3	23.8	5.2
Mix 7	29.8	3.5	44.6	10.6	33.1	1.7
Mix 8	36.0	3.1	59.6	3.5	37.1	13.4
Mix 9	25.2	1.2	37.3	14.1	30.6	7.2
Mix 10	32.3	4.0	48.8	2.1	37.5	2.0
Mix 11	35.6	13.3	60.3	31.1	37.5	1.0
Mix 12	31.5	5.5	28.5	12.7	27.9	11.0
Mix 13	23.8	7.0	33.4	4.9	27.3	2.5
Mix 14	40.0	2.6	48.1	19.1	35.4	2.5
Mix 15	34.2	7.2	36.9	4.9	27.3	5.5

3.4. Correlations between porosity, chemical composition, crack complexity, and self-healing efficiency

Pearson's linear correlation coefficient (*r*) was calculated to examine the relations between phase composition (calcite, Portlandite, Si/Ca), microstructure (porosity), initial crack geometry (ICA, T, FD, MCW, ACW), and self-healing efficiency (CSR, CC, IR25, IR180, SR25). The values of *r* are presented in Figs. 23 and 24. Depending on the number of observation pairs, the statistical significance of the correlation coefficients were calculated at the significance level $\alpha = 0.05$. The statistically significant intervals are marked in Figs. 23 and 24 for each group of correlation coefficients.

The correlation results suggest that a higher porosity of the hardened paste leads to a more effective internal self-healing which can be related to the improved transport properties (lower IR180 and IR25) (Fig. 23c). Higher porosity, especially open/capillary porosity, presumably facilitates the transport of ions, Ca, Al, and Si, into the crack. Nevertheless, the microstructure porosity is not correlated with strength recovery (CSR80/100, Fig. 23a). Here, presumably, other factors govern the self-healing process, e.g., the phase composition of the hardened binder. For instance, the higher the calcite amount, i.e., limestone content, the higher the strength regain (Fig. 23b), especially for more damaged samples (CSR100). Wider cracks formed due to loading mean a more interconnected crack network, presumably leading to more accessible ion/water transport. It is essential to mention that the porosity determination has limitations due to the 2D character of the analysis. Since concrete's porous network is complex, it requires further testing with different imaging methods, e.g., X-ray microtomography. Also, the role of the different pore sizes and the tortuosity in transporting ions through the cementitious matrix could be significant [11].

For the self-healing at the crack mouth, associated with the calcium carbonate precipitation mechanism, a moderate negative correlation is visible between the Portlandite and the crack closure CC (Fig. 23b). It suggests that the more Portlandite available in the binder matrix, the smaller the surface crack closure. Similarly, for the internal self-healing related to calcium carbonate precipitation and ongoing hydration, a
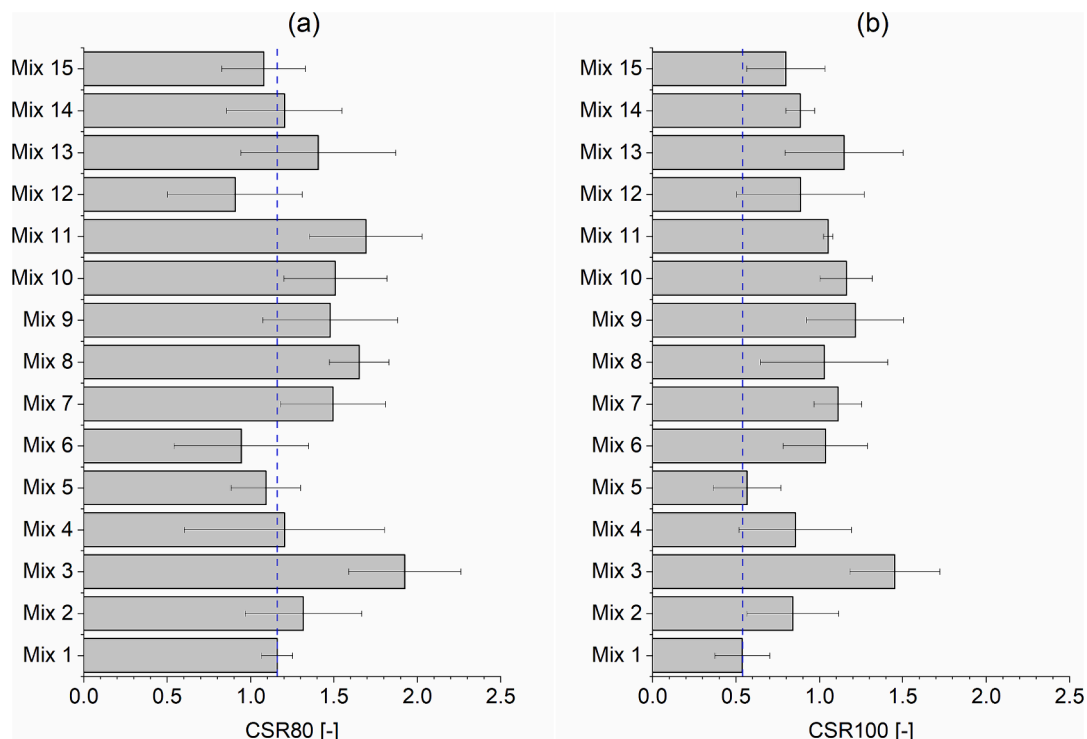

Fig. 17. Compressive strength regain for all the mixes after self-healing: (a) after 80% damage (CSR80), (b) after 100% damage (CSR100).
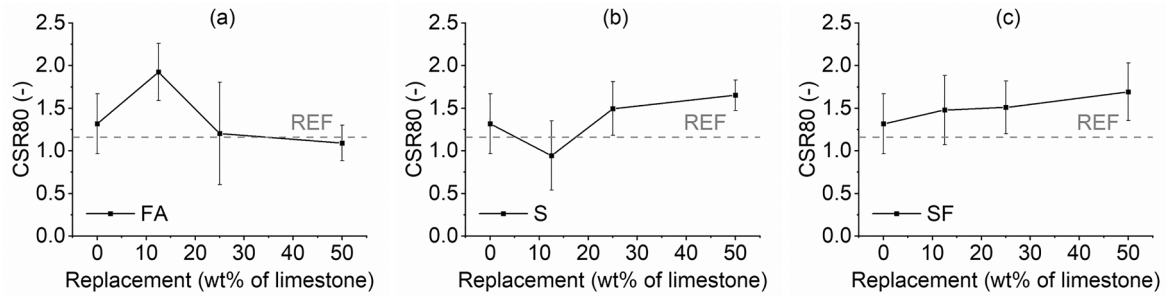
Fig. 18. Changes of compressive strength regain after 80% damage (CSR 80) with the wt % limestone replacement with (a) FA, (b) S, and (c) SF.
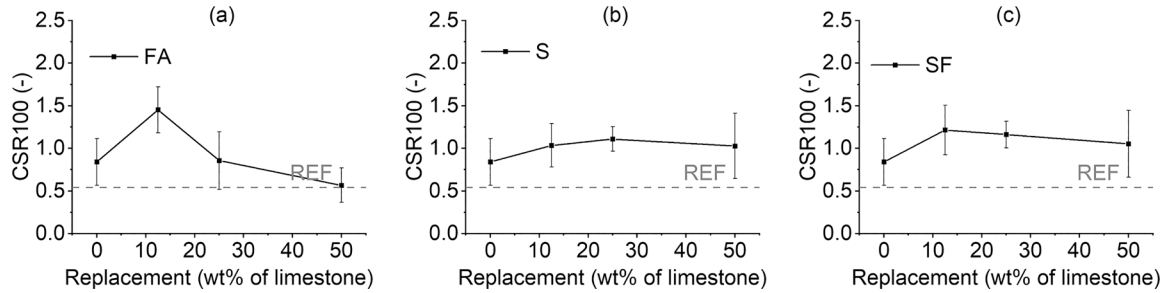

Fig. 19. Changes of compressive strength regain after 100% damage (CSR 100) with the wt % limestone replacement with (a) FA, (b) S, and (c) SF.
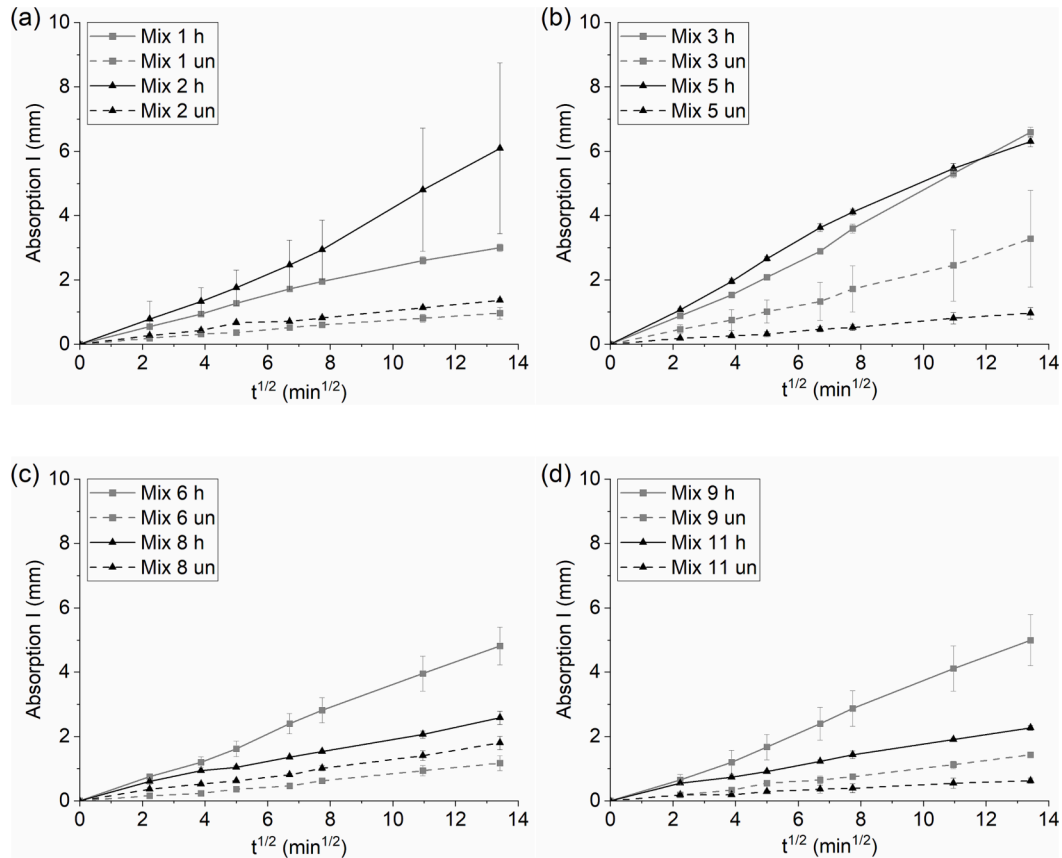

Fig. 20. Measured water absorption curves (h – healed, un – undamaged specimen) for (a) REF (Mix 1) and LM50 (Mix 2), (b) LM43.75 FA6.25 (Mix 3) and LM25 FA25 (Mix 5), (c) LM43.75 S6.25 (Mix 6) and LM25 S25 (Mix 8), (d) LM43.75 SF6.25 (Mix 9) and LM25 SF25 (Mix 11).

moderate positive correlation is visible between the presence of Portlandite and the transport properties of the solidified binder matrix (IR180, IR25) (Fig. 23d). It could suggest that the higher the amount of

Portlandite, the less efficient healing happens. Based on the obtained results, it could be concluded that the Portlandite is not critical, and other factors presumably influence these relations, e.g., the amount of
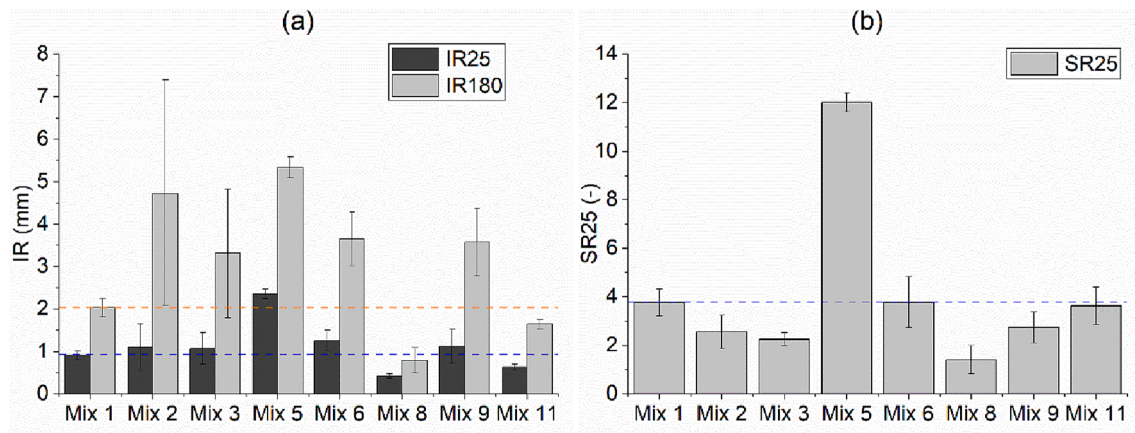
Fig. 21. (a) Water absorption recovery at 25 and 180 min (IR25 and IR180), (b) Sorptivity change during 25 min (SR25).
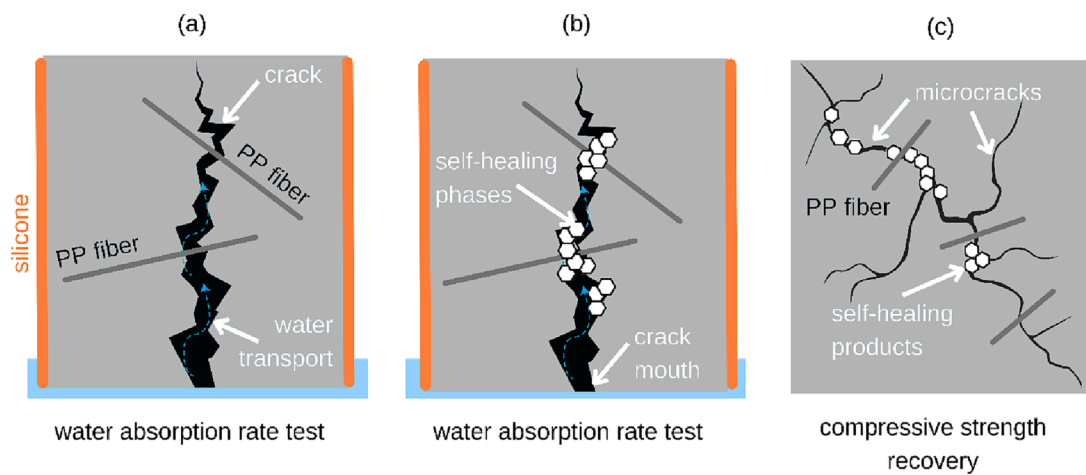

Fig. 22. (a) fiber effect on water absorption rate, (b) internal healing effect on water absorption rate, (c) internal healing effect on strength recovery.

unhydrated binder or the environmental exposure.

Nevertheless, an essential factor that affected the analysis is the lack of maturity of the studied binders. A lower initial amount of Portlandite, observed, e.g., for silica fume specimens (Mixes 9–11) (Table 3), could indicate that most SF has already reacted with Portlandite through the pozzolanic reaction forming C-S-H. Therefore, the remaining $Ca(OH)_2$ could contribute to self-healing by providing calcium ions inside the crack. On the other hand, all limestone-fly ash systems (Mixes 3–5), with a slower reaction rate, contained a high amount of Portlandite at the moment of cracking. This Portlandite was gradually consumed during the self-healing period due to a pozzolanic reaction; hence, the amount of $Ca(OH)_2$ contributing to recovery was possibly low, especially for high volumes of fly ash (Mixes 4 and 5).

Correlation analysis indicated that geometrical complexity characterized by FD and T of the crack does not affect the external CC (Fig. 24b). However, the FD and MCW are correlated with the recovery of transport properties, indicating internal healing of the crack (Fig. 24a, Fig. 25cd). The more complex the crack and the wider the crack, the less efficient the healing. A low correlation between the CC and maximum and average crack width can also be seen. Nevertheless, the low variability of tortuosity and FD could be a problem; therefore, a wider range of cracking complexity parameters should be studied for the same mix chemistry.

3.5. Effect of binder composition

Comparing the overall performance of the limestone-SCM binders,

several mixes showed better self-healing efficiency than pure OPC or OPC/limestone blended binders. The enhancement could presumably be linked to a synergistic effect between the limestone and the mineral additions at an early age [15] (Siad et al., 2015). Limestone increases the reactivity of cement due to the nucleation site effect, leading to faster production of Portlandite and increased pozzolanic reactions at an early age [15]. Nevertheless, further research should be conducted to verify this phenomenon in the self-healing process and its potential at later ages.

Several different self-healing behaviors were observed based on the combination of analyzed efficiency parameters. This is clearly demonstrated on the radar plots in Fig. 26, showing a comparison among selected samples with limestone/fly ash (Mixes 3 and 5), limestone/slag (Mixes 6 and 8), and limestone/silica fume (Mixes 9 and 1) mixed in different proportions. Data in Fig. 26 are normalized by each characteristic's maximum and minimum values. It is evident from these graphs that the F25 S25 (Mix 8) binder has the best combination of self-healing properties (i.e., crack closure, compressive strength recovery, and water absorption), measured as the proportional area of the radar plots.

Differences in self-healing can be presumably attributed to the fact that transport processes in cementitious materials are related to their microstructure which includes three major components: the assemblage of solid phases, pore structure, and pore solution composition [67]. Each of these components varies with the use of different SCMs.

Silica fume affects the characteristics of both C-S-H and Portlandite (CH) phases. CH grows in the gaps between the grains and the hydration shell. Also, the pore solution is calcium-rich at early ages, but later
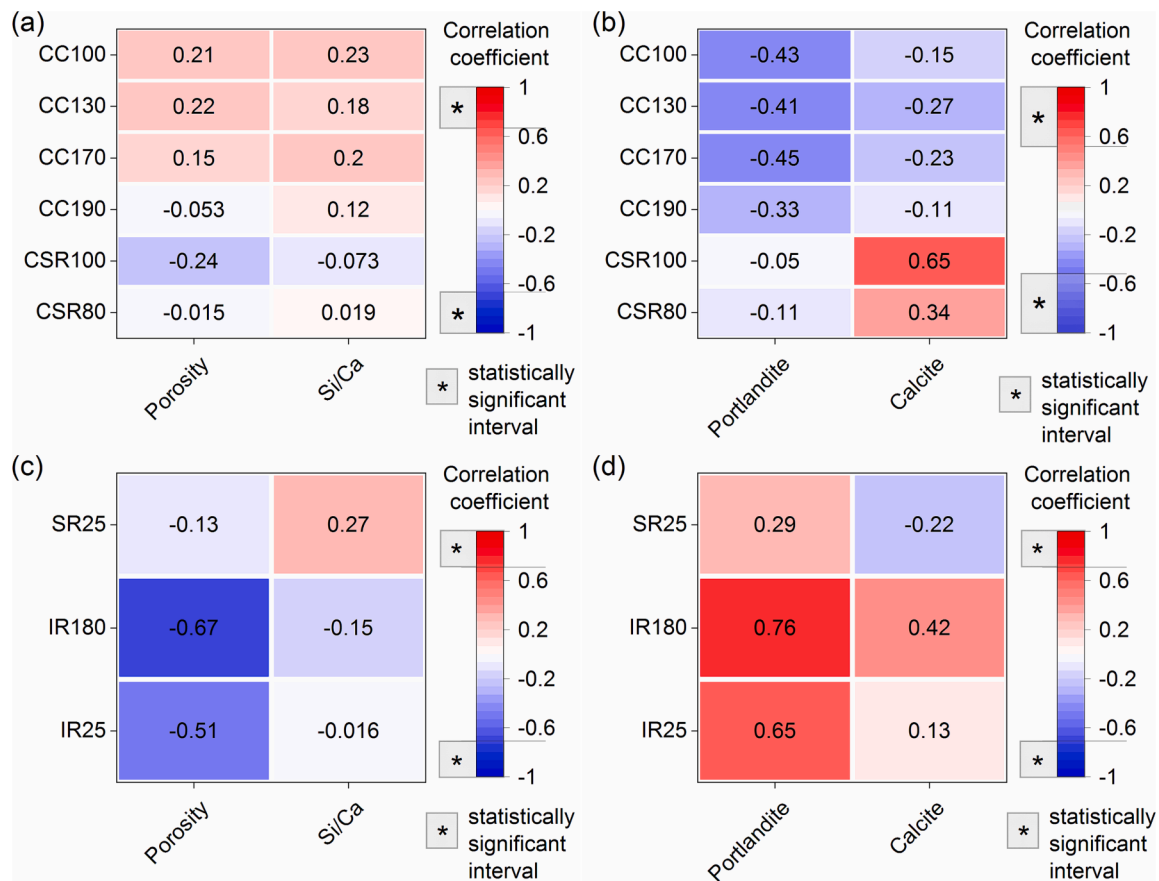
Fig. 23. Pearson's linear correlation coefficients (*r*) between microstructure parameters/chemical composition and self-healing efficiency.
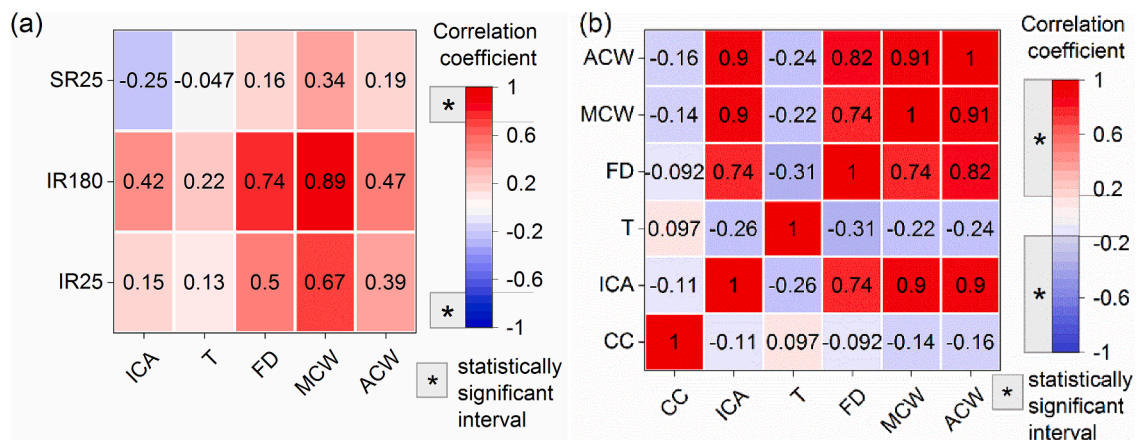

Fig. 24. Pearson's linear correlation coefficients (r) between initial crack geometrical parameters and self-healing efficiency.

silicon dominates [68]. Therefore, more silicon in the inner C-A-S-H (higher Si/Ca ratio) and higher porosity could suggest internal healing with primarily C-S-H phases and a limited amount of $CaCO_3$ sealing the crack externally, resulting in a low crack closure but high strength and water absorption recovery.

Low-calcium fly ash applied in this study is characterized by a slow reaction rate and high activation energy. However, adding limestone accelerates the reaction and lowers the apparent activation energy [69]). Nevertheless, high quantities of fly ash (as in mix LM25 FA25) react slower (Lottenbach et al. 2011); therefore, the microstructure and chemical composition of this binder formulation is not "mature" at 7 days. Furthermore, the consumption of Portlandite in the pozzolanic reaction increases after 1 week (Lottenbach et al. 2011); therefore, there might not have been enough calcium released into the crack for the self-healing process since Portlandite was depleted. In addition, the water solution inside the crack cannot activate the hydration of unreacted FA particles due to their low reactivity [18]. Since the instability of the FA systems investigated in this study could have implications for the results, further research should be focused on analyzing the self-healing behavior at different cracking ages.

Slag binders exhibit similar behavior as Portland cement. However, slag does not fully hydrate [12]; therefore, self-healing based on an ongoing hydration mechanism is possible. The continued hydration of slag inside the crack is possible due to its higher hydration activity and
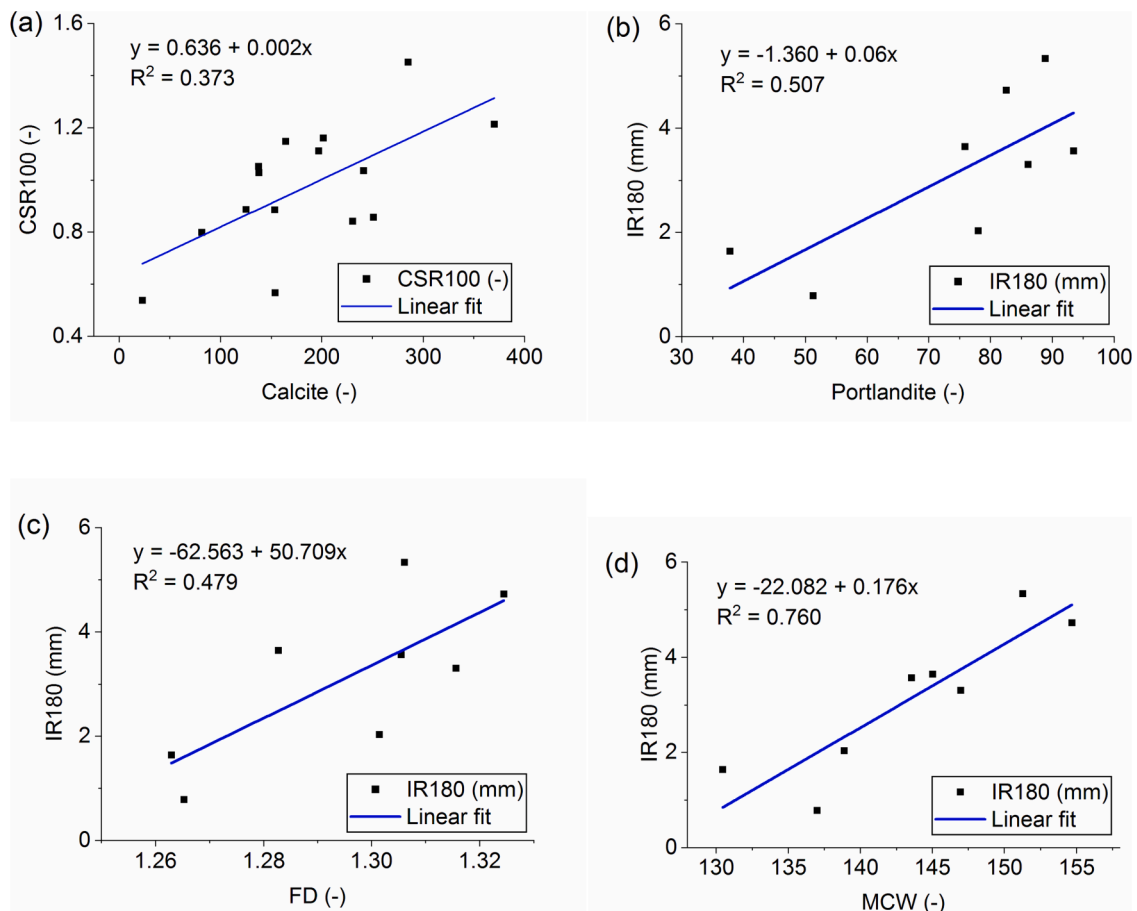
Fig. 25. Most significant correlations with linear fit: (a) Calcite vs. CSR100, (b) Portlandite vs. IR180, (c) FD vs. IR180, and (d) MCW vs. IR180.
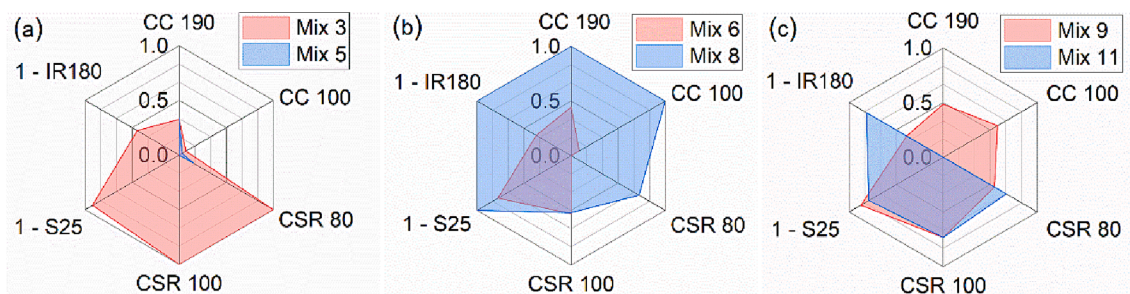

Fig. 26. Radar plots showing a comparison among selected mixes: (a) LM43.75 FA6.25 (Mix 3) and LM25 FA25 (Mix 5), (b) LM43.75 S6.25 (Mix 6) and LM25 S25 (Mix 8), (c) LM43.75 SF6.25 (Mix 9) and LM25 SF25 (Mix 11). Data are normalized by the maximum and minimum values of each parameter.

higher CaO content than, e.g., fly ash. In addition, a limestone content between 20 and 50 wt-% increases the slag efficiency [70], which could contribute to its superior self-healing behavior.

The pore solution effect on the self-healing is presumably related to the ion concentrations (e.g., Ca^{2+}) and the solution's pH. Calcium concentration in the pore solution tends to decrease at high FA and slag replacement levels [71] which can possibly slow down the blended binders' reaction within the crack. A more extended healing period, with a prolonged "wetting" phase, could potentially increase the dissolution/transport of the ions within the crack and increase the pH of the crack solution leading to higher crack closure. The higher pH of the pore solution facilitates the disassociation of the carbonic acid inside the crack, which reacts with calcium ions to form calcium carbonate crystals (Yildirim et al., 2015).

The crack closure for most limestone-SCM blended binders was

higher than the reference OPC specimen (Fig. 16); however still relatively low, especially for fly ash systems, and reaching a maximum of 60% for slag and 40% for silica fume specimens, which could be related to an early age of the samples. It can be speculated that the unreacted SCM particles consumed the Portlandite in the pozzolanic reaction to form additional C-S-H. This affected the self-healing mechanism by decreasing the carbonation/calcite formation at the surface of the crack [17]. The amount of Portlandite in the matrix was hypothesized as one of the constituents promoting the self-healing process by providing the Ca^{2+} ions, which are transported into the crack where they react with water and carbon dioxide, forming calcium carbonate crystals sealing the crack (e.g., [4]). Here, the amount of Portlandite does not positively correlate with the healing efficiency. Once more, the results could be related to the early age of the cracking, i.e., 7 days. Selected binder components, e.g., fly ash, react slower and consume Portlandite in a

pozzolanic reaction, leading to less Portlandite available for the self-healing process. The reaction speed is different for each binder combination; therefore, the Portlandite effect on self-healing is inconclusive and requires further studies.

The applied binders display distinct pore network features, which are not directly visible based on the calculated total porosity value. Fly ash blends exhibit low porosity; however, the high sorptivity coefficient value for undamaged specimens of Mix 3 (LM43.75 FA6.25) indicates possibly high capillary (open) porosity [11]. Permeable binder matrix could be linked to a good self-healing performance of this binder [4] compared to Mix 5 (LM25 FA25), where this effect was not present (Fig. 20b). LM25 FA25 was characterized by low total porosity and low connectivity of pores based on the high sorptivity coefficient (Fig. 21b), which could presumably cause problems with the transport of the ions into the crack and, consequently, unsatisfactory crack repair.

Even though small amounts of silica fume generally lead to a decreased porosity of limestone-blended biners, adding over 8 wt% of silica fume causes a porosity increase [72], which is in agreement with this study (Fig. 12). Nevertheless, a discontinuous pore structure attributes to a lower permeability [72]. In addition, the outer C-A-S-H product is more homogenous in hydrated binders containing silica fume, exhibiting reduced capillary porosity [68], which could justify the limited external crack closure (Fig. 16c) for the LM25 SF25 mix (Mix 11).

Finally, the formation of morphologically- and chemically different self-healing products inside the crack could also possibly hinder the reaction. For instance, C-S-H is speculated to limit material's water absorption by depercolating capillaries and simultaneously participating in the transport of ions [11]. Therefore, more in-depth studies of phase assemblage inside the crack should be performed.

4. Conclusions

In this study, an exhaustive evaluation of the early-age self-healing performance of the limestone-rich multi-component cementitious binders was performed. The dependence of the healing on the microstructural properties and chemical composition of the hydrated binder was studied. In addition, the effect of the initial crack geometry on the healing process was also analyzed. Several self-healing descriptors were used to characterize the efficiency of the process, i.e., crack closure ratio, sorptivity coefficient, and strength recovery.

The following main conclusions could be drawn from this study:

- Several limestone-SCM cementitious materials showed better self-healing efficiency than pure OPC or OPC-limestone blends. A synergistic effect between the limestone and the mineral additions could facilitate the recovery at an early age; however, more detailed studies should be conducted to confirm this relationship.
- Binder composition affected the self-healing mechanism leading to different levels of performance recovery. Replacement of cement with 25% of limestone and 25% of slag (mix LM25 S25) demonstrated an outstanding combination of self-healing properties (i.e., crack closure, compressive strength recovery, and water absorption),
- The portlandite amount had a higher correlation with the crack closure (CC) than with the strength regain (CSR80, CSR100), contrary to the limestone amount. A smaller amount of Portlandite resulted in more efficient self-healing. A higher amount of limestone in the hardened binder matrix led to a significantly higher strength regain due to the self-healing process.
- Correlation analysis indicated that the geometrical complexity characterized by FD and T of the crack did not affect the external crack closure (CC). However, the FD and MCW were correlated with the transport properties. Therefore, the more complex and wider the crack, the less efficient healing could be expected.

The following limitations and possible further research directions were indicated:

- This exploratory study was aimed at preliminary estimating the self-healing potential of ternary and quaternary mortar mixes with high amounts of limestone combined with SCMs. In addition, binary mixes should also be tested to verify the possible synergy between limestone and SCMs.
- Completed research considered early-age binders to potentially obtain improved self-healing behavior due to the ongoing hydration mechanism. Nevertheless, in the case of low reactivity binders, e.g., class F fly ash, the microstructure and chemical composition change significantly at an early age due to pozzolanic reaction. Therefore, evaluating the self-healing performance of mortars cracked at later ages, when the mature material is more "stable," should be considered.
- Performed self-healing efficiency evaluation compared the healed specimen's performance with the intact state, i.e., the strength recovery and water absorption rate measurements. A comparison with the damaged state could be investigated to gain additional insights into the self-healing performance.
- Since the overall crack closure measured at the surface was relatively low, other self-healing exposures could be tested to improve the self-healing process. It could be speculated that for the ongoing hydration mechanism, a more prolonged wetting phase would be beneficial. Further optimization of the healing conditions should be performed.

CRediT authorship contribution statement

Magdalena Rajczakowska: Conceptualization, Data curation, Formal analysis, Investigation, Methodology, Software, Validation, Visualization, Writing – original draft. **Ilda Tole:** Methodology, Software, Data curation, Writing – review & editing. **Hans Hedlund:** Supervision, Funding acquisition. **Karin Habermehl-Cwirzen:** Supervision, Writing – review & editing. **Andrzej Cwirzen:** Funding acquisition, Project administration, Supervision, Writing – review & editing.

Declaration of Competing Interest

The authors declare that they have no known competing financial interests or personal relationships that could have appeared to influence the work reported in this paper.

Data availability

Data will be made available on request.

Acknowledgments

References

[1] X. Cao, X. Dai, J. Liu, Building energy-consumption status worldwide and the state-of-the-art technologies for zero-energy buildings during the past decade, Energ. Buildings 128 (2016) 198–213.

[2] M.K. Dixit, Life cycle recurrent embodied energy calculation of buildings: A review, J. Clean. Prod. 209 (2019) 731–754.

[3] W. Zhang, Q. Zheng, A. Ashour, B. Han, Self-healing cement concrete composites for resilient infrastructures: A review, Compos. B Eng. 189 (2020), 107892.

[4] M. Rajczakowska, K. Habermehl-Cwirzen, H. Hedlund, A. Cwirzen, The effect of exposure on the autogenous self-healing of ordinary Portland cement mortars, Materials 12 (23) (2019) 3926.

[5] B. Van Belleghem, P. Van den Heede, K. Van Tittelboom, N. De Belie, Quantification of the service life extension and environmental benefit of chloride exposed self-healing concrete, Materials 10 (1) (2017) 5.

[6] Wolfs, R., & Salet, T. (2016). Potentials and challenges in 3D concrete printing. In Proc., 2nd Int. Conf. on Progress in Additive Manufacturing (pp. 8-13).

[7] K.L. Scrivener, V.M. John, E.M. Gartner, Eco-efficient cements: Potential economically viable solutions for a low-CO2 cement-based materials industry, Cem. Concr. Res. 114 (2018) 2–26.

[8] IEA, WBCSD, Cement Technology Road-map 2009 Carbon Emissions Reductions up to 2050, OECD/IEA:; WBCSD, Paris:; Conches-Geneva, Switzerland (2009).

[9] M. Karimpour, M. Belusko, K. Xing, F. Bruno, Minimising the life cycle energy of buildings: Review and analysis, Build. Environ. 73 (2014) 106–114.

[10] M. Rajczakowska, L. Nilsson, K. Habermehl-Cwirzen, H. Hedlund, A. Cwirzen, Does a High Amount of Unhydrated Portland Cement Ensure an Effective Autogenous Self-Healing of Mortar? Materials 12 (20) (2019) 3298.

[11] Durdziński, P. T. (2016). Hydration of multi-component cements containing cement clinker, slag, calcareous fly ash and limestone (No. THESIS). EPFL.

[12] B. Lothenbach, G. Le Saout, E. Gallucci, K. Scrivener, Influence of limestone on the hydration of Portland cements, Cem. Concr. Res. 38 (6) (2008) 848–860.

[13] G.V.B.B. Menéndez, V. Bonavetti, E.F. Irassar, Strength development of ternary blended cement with limestone filler and blast-furnace slag, Cem. Concr. Compos. 25 (1) (2003) 61–67.

[14] S. Sharma, S. Bishnoi, F. Martirena, K. Scrivener, Limestone calcined clay cement and concrete: A state-of-the-art review, Cem. Concr. Res. 149 (2021) 106564.

[15] P. Mounanga, M.I.A. Khokhar, R. El Hachem, A. Loukili, Improvement of the early-age reactivity of fly ash and blast furnace slag cementitious systems using limestone filler, Mater. Struct. 44 (2) (2011) 437–453.

[16] H. Chang, C. Li, J. Wang, H. Zhang, Z. Ge, Z. Zuo, J. Liu, Y. Zhou, The features of different mineral admixtures affecting the self-healing capacity of cementitious-based materials, Constr. Build. Mater. 297 (2021) 123822.

[17] R. Maddalena, H. Taha, D. Gardner, Self-healing potential of supplementary cementitious materials in cement mortars: Sorptivity and pore structure, Develop. Built Environ. 6 (2021) 100044.

[18] M. Luo, K. Jing, J. Bai, Z. Ding, D. Yang, H. Huang, Y. Gong, Effects of curing conditions and supplementary cementitious materials on autogenous self-healing of early age cracks in cement mortar, Crystals 11 (7) (2021) 752.

[19] T.H. Ahn, T. Kishi, Crack self-healing behavior of cementitious composites incorporating various mineral admixtures, J. Adv. Concr. Technol. 8 (2) (2010) 171–186.

[20] H. Huang, G. Ye, D. Damidot, Effect of blast furnace slag on self-healing of microcracks in cementitious materials, Cem. Concr. Res. 60 (2014) 68–82.

[21] K. Van Tittelboom, E. Gruyaert, H. Rahier, N. De Belie, Influence of mix composition on the extent of autogenous crack healing by continued hydration or calcium carbonate formation, Constr. Build. Mater. 37 (2012) 349–359.

[22] C.Y. Namnoum, B. Hilloulin, F. Grondin, A. Loukili, Determination of the origin of the strength regain after self-healing of binary and ternary cementitious materials including slag and metakaolin, J. Build. Eng. 41 (2021), 102739.

[23] M. Mohammadi, C. Youssef-Namnoum, M. Robira, B. Hilloulin, Self-Healing Potential and Phase Evolution Characterization of Ternary Cement Blends, Materials 13 (11) (2020) 2543.

[24] J. Qiu, H.S. Tan, E.H. Yang, Coupled effects of crack width, slag content, and conditioning alkalinity on autogenous healing of engineered cementitious composites, Cem. Concr. Compos. 73 (2016) 203–212.

[25] H.L. Wang, J.G. Dai, X.Y. Sun, X.L. Zhang, Characteristics of concrete cracks and their influence on chloride penetration, Constr. Build. Mater. 107 (2016) 216–225.

[26] A. Akhavan, S.-M.-H. Shafaatian, F. Rajabipour, Quantifying the effects of crack width, tortuosity, and roughness on water permeability of cracked mortars, Cem. Concr. Res. 42 (2) (2012) 313–320.

[27] M. Szeląg, Fractal characterization of thermal cracking patterns and fracture zone in low-alkali cement matrix modified with microsilica, Cem. Concr. Compos. 114 (2020) 103732.

[28] K. Scrivener, F. Martirena, S. Bishnoi, S. Maity, Calcined clay limestone cements (LC3), Cem. Concr. Res. 114 (2018) 49–56.

[29] H.e. Zhu, D. Zhang, T. Wang, H. Wu, V.C. Li, Mechanical and self-healing behavior of low carbon engineered cementitious composites reinforced with PP-fibers, Constr. Build. Mater. 259 (2020) 119805.

[30] R. Gettu, A. Patel, V. Rathi, S. Prakasan, A.S. Basavaraj, S. Palaniappan, S. Maity, Influence of supplementary cementitious materials on the sustainability parameters of cements and concretes in the Indian context, Mater. Struct. 52 (1) (2019) 1–11.

[31] E. Jamieson, B. McLellan, A. Van Riessen, H. Nikraz, Comparison of embodied energies of Ordinary Portland Cement with Bayer-derived geopolymer products, J. Clean. Prod. 99 (2015) 112–118.

[32] R.L. Sharma, S.P. Pandey, Influence of mineral additives on the hydration characteristics of ordinary Portland cement, Cem. Concr. Res. 29 (9) (1999) 1525–1529.

[33] S. Catinaud, J.J. Beaudoin, J. Marchand, Influence of limestone addition on calcium leaching mechanisms in cement-based materials, Cem. Concr. Res. 30 (12) (2000) 1961–1968.

[34] L. Courard, F. Michel, Limestone fillers cement based composites: Effects of blast furnace slags on fresh and hardened properties, Constr. Build. Mater. 51 (2014) 439–445.

[35] D.P. Bentz, Modeling the influence of limestone filler on cement hydration using CEMHYD3D, Cem. Concr. Compos. 28 (2) (2006) 124–129.

[36] T. Nishiwaki, S. Kwon, D. Homma, M. Yamada, H. Mihashi, Self-Healing Capability of Fiber-Reinforced Cementitious Composites for Recovery of Watertightness and Mechanical Properties, Materials 7 (3) (2014) 2141–2154.

[37] EN 1015-11-2019 Methods of test for mortar for masonry Part 11: Determination of flexural and compressive strength of hardened mortar.

[38] C. Edvardsen, Water permeability and autogenous healing of cracks in concrete, in: Innovation in concrete structures: Design and construction, Thomas Telford Publishing, 1999, pp. 473–487.

[39] M. Roig-Flores, S. Moscato, P. Serna, L. Ferrara, Self-healing capability of concrete with crystalline admixtures in different environments, Constr. Build. Mater. 86 (2015) 1–11.

[40] R. Gagné, M. Argouges, A study of the natural self-healing of mortars using air-flow measurements, Mater. Struct. 45 (11) (2012) 1625–1638.

[41] E. Ahn, H. Kim, B. Park, M. Shin, Long-term autogenous healing and re-healing performance in concrete: Evaluation using air-coupled surface-wave method, Constr. Build. Mater. 307 (2021) 124939.

[42] F. Adenot, M. Buil, Modelling of the corrosion of the cement paste by deionized water, Cem. Concr. Res. 22 (2–3) (1992) 489–496.

[43] J. Schindelin, I. Arganda-Carreras, E. Frise, V. Kaynig, M. Longair, T. Pietzsch, S. Preibisch, C. Rueden, S. Saalfeld, B. Schmid, J.-Y. Tinevez, D.J. White, V. Hartenstein, K. Eliceiri, P. Tomancak, A. Cardona, Fiji: an open-source platform for biological-image analysis, Nat. Methods 9 (7) (2012) 676–682.

[44] J. Sauvola, M. Pietikäinen, Adaptive document image binarization, Pattern Recogn. 33 (2) (2000) 225–236.

[45] ASTM C1585-20 – Standard Test Method for Measurement of Rate of Absorption of Water by Hydraulic-Cement Concretes.

[46] Z. Zhang, S. Qian, H. Ma, Investigating mechanical properties and self-healing behavior of micro-cracked ECC with different volume of fly ash, Constr. Build. Mater. 52 (2014) 17–23.

[47] S. Gupta, H.W. Kua, S. Dai Pang, Healing cement mortar by immobilization of bacteria in biochar: An integrated approach of self-healing and carbon sequestration, Cem. Concr. Compos. 86 (2018) 238–254.

[48] F. Georget, W. Wilson, K.L. Scrivener, edxia: Microstructure characterisation from quantified SEM-EDS hypermaps, Cem. Concr. Res. 141 (2021) 106327.

[49] R. Snellings, J. Chwast, Ö. Cizer, N. De Belie, Y. Dhandapani, P. Durdzinski, J. Elsen, J. Haufe, D. Hooton, C. Patapy, M. Santhanam, K. Scrivener, D. Snoeck, L. Steger, S. Tongbo, A. Vollpracht, F. Winnefeld, B. Lothenbach, RILEM TC-238 SCM recommendation on hydration stoppage by solvent exchange for the study of hydrate assemblages, Mater. Struct. 51 (6) (2018).

[50] H.S. Wong, M.K. Head, N.R. Buenfeld, Pore segmentation of cement-based materials from backscattered electron images, Cem. Concr. Res. 36 (6) (2006) 1083–1090.

[51] J. Schindelin, C.T. Rueden, M.C. Hiner, K.W. Eliceiri, The ImageJ ecosystem: An open platform for biomedical image analysis, Mol. Reprod. Dev 82 (7-8) (2015) 518–529.

[52] C.T. Rueden, J. Schindelin, M.C. Hiner, B.E. DeZonia, A.E. Walter, E.T. Arena, K. W. Eliceiri, Image J2: ImageJ for the next generation of scientific image data, BMC Bioinf. 18 (1) (2017) 1–26.

[53] J.E. Rossen, K.L. Scrivener, Optimization of SEM-EDS to determine the C-A-S-H composition in matured cement paste samples, Mater Charact 123 (2017) 294–306.

[54] T. Hildebrand, P. Rüegsegger, A new method for the model-independent assessment of thickness in three-dimensional images, J. Microsc. 185 (1) (1997) 67–75.

[55] T. Saito, J.I. Toriwaki, New algorithms for euclidean distance transformation of an n-dimensional digitized picture with applications, Pattern Recogn. 27 (11) (1994) 1551–1565.

[56] Y.S. Wu, L.J. van Vliet, H.W. Frijlink, K. van der Voort Maarschalk, The determination of relative path length as a measure for tortuosity in compacts using image analysis, Eur. J. Pharm. Sci. 28 (5) (2006) 433–440.

[57] I. Arganda-Carreras, R. Fernández-González, A. Muñoz-Barrutia, C. Ortiz-De-Solorzano, 3D reconstruction of histological sections: Application to mammary gland tissue, Microsc. Res. Tech. 73 (11) (2010) 1019–1029.

[58] T.C. Lee, R.L. Kashyap, C.N. Chu, Building skeleton models via 3-D medial surface axis thinning algorithms. CVGIP, Graphical Models and Image Processing 56 (6) (1994) 462–478.

[59] J. Li, Q. Du, C. Sun, An improved box-counting method for image fractal dimension estimation, Pattern Recogn. 42 (11) (2009) 2460–2469.

[60] K. Foroutan-pour, P. Dutilleul, D.L. Smith, Advances in the implementation of the box-counting method of fractal dimension estimation, Appl. Math Comput. 105 (2–3) (1999) 195–210.

[61] A. Karperien, FracLac for ImageJ. http://rsb.info.nih.gov/ij/plugins/fraclac/FLHelp/Introduction.htm, 1999-2013.

[62] A. Beglarigale, D. Eyice, B. Tutkun, H. Yazıcı, Evaluation of enhanced autogenous self-healing ability of UHPC mixtures, Constr. Build. Mater. 280 (2021) 122524.

[63] M.K. Gopalan, Nucleation and pozzolanic factors in strength development of class fly ash concrete, Mater. J. 90 (2) (1993) 117–121.

[64] H. Toutanji, N. Delatte, S. Aggoun, R. Duval, A. Danson, Effect of supplementary cementitious materials on the compressive strength and durability of short-term cured concrete, Cem. Concr. Res. 34 (2) (2004) 311–319.

[65] W. Zhong, W. Yao, Influence of damage degree on self-healing of concrete, Constr. Build. Mater. 22 (6) (2008) 1137–1142.

[66] J. Feng, Y. Su, C. Qian, Coupled effect of PP fiber, PVA fiber and bacteria on self-healing efficiency of early-age cracks in concrete, Constr. Build. Mater. 228 (2019) 116810.

[67] S. Sui, F. Georget, H. Maraghechi, W. Sun, K. Scrivener, Towards a generic approach to durability: Factors affecting chloride transport in binary and ternary cementitious materials, Cem. Concr. Res. 124 (2019) 105783.

[68] J.E. Rossen, B. Lothenbach, K.L. Scrivener, Composition of C-S–H in pastes with increasing levels of silica fume addition, Cem. Concr. Res. 75 (2015) 14–22.

[69] D.P. Bentz, Activation energies of high-volume fly ash ternary blends: Hydration and setting, Cem. Concr. Compos. 53 (2014) 214–223.

[70] T. Proske, M. Rezvani, S. Palm, C. Müller, C.A. Graubner, Concretes made of efficient multi-composite cements with slag and limestone, Cem. Concr. Compos. 89 (2018) 107–119.

[71] A. Vollpracht, B. Lothenbach, R. Snellings, J. Haufe, The pore solution of blended cements: a review, Mater. Struct. 49 (8) (2016) 3341–3367.

[72] J. Zelić, R. Krstulović, E. Tkalčec, P. Krolo, The properties of Portland cement-limestone-silica fume mortars, Cem. Concr. Res. 30 (1) (2000) 145–152.